REVIEW ARTICLE OPEN

2D materials for spintronic devices

Ethan C. Ahn[1]✉

2D materials are attractive for nanoelectronics due to their ultimate thickness dimension and unique physical properties. A wide variety of emerging spintronic device concepts will greatly benefit from the use of 2D materials, leading a better way to manipulating spin. In this review, we discuss various 2D materials, including graphene and other inorganic 2D semiconductors, in the context of scientific and technological advances in spintronic devices. Applications of 2D materials in spin logic switches, spin valves, and spin transistors are specifically investigated. We also introduce the spin-orbit and spin-valley coupled properties of 2D materials to explore their potential to address the crucial issues of contemporary electronics. Finally, we highlight major challenges in integrating 2D materials into spintronic devices and provide a future perspective on 2D materials for spin logic devices.

npj 2D Materials and Applications (2020)4:17 ; https://doi.org/10.1038/s41699-020-0152-0

INTRODUCTION

The unprecedented success of silicon-CMOS technology has been primarily driven by transistor scaling. The early era of Dennard scaling[1,2] had two important consequences for modern computing systems; speed performance has been improved by scaling of physical dimensions while power density has been kept practically constant by scaling of voltages. However, since around 2005, the voltage scaling has become a challenging task[3] because further reduction of the supply voltage (requiring the threshold voltage to be simultaneously decreased to maintain the capability to drive high current) was leading to an exponential increase in the leakage current. This is due to the fundamental limit of subthreshold swing (SS) greater than 60 mV/decade at room temperature, which arises from the Boltzmann statistics that govern the thermionic operation of conventional MOSFETs[4]. Although tunnel FETs[5–7], negative capacitance FETs[8–10], and electrostrictive FETs[11,12] have recently emerged as novel device concepts for steep SS, they still require much work to improve the device performance and/or answer fundamental questions on scalability, reliability, and viability. On the other hand, scaling of physical dimensions still continued until today, towards the technology nodes of 5 nm and beyond[13,14]. This led to an inevitable increase in power density in high-performance microprocessors, thus requiring complex power management techniques[15,16]. In view of this, spintronics, which utilizes the quantum mechanical property of elementary particles, called spin, has the potential to become an innovative pathway beyond transistor scaling to satisfying the speed and energy-efficiency needs of the emerging computing paradigm (e.g., neuromorphic[17,18] or quantum[19,20] computing).

Spintronics is an emerging form of electronics that harnesses the intrinsic angular momentum (spin) of electrons, leading researchers to treat them as tiny bar magnets with strong magnetic moment (Bohr magneton, $\mu_B \sim 10^{-23}$ Am^2). Immediately after the discovery of giant magnetoresistance (GMR) in 1988 (the GMR ratio of 10–50%, as compared with the anisotropic MR effect of at most a few percent at that time)[21,22], which has been the foundation for constructing the hard-drive read head, research on nanomagnetism and spintronics has made remarkable strides over the last few decades. In 1991, the oscillatory behavior of the interlayer exchange coupling was formulated in terms of the Fermi surface of the spacer material[23,24], leading a way to constructing a synthetic magnetic free layer in the modern magnetic tunnel junction (MTJ) device[25,26]. The concept of "spin valve" ignited numerous research efforts exploring the ferromagnetic sandwiches spaced by a nonmagnetic metallic layer[27,28]; logical "1" or the high-resistance state is represented by the antiparallel configuration of two ferromagnetic layers while logical "0" or the low-resistance state is dictated by the parallel configuration. This is an important milestone in spintronics because spin valve currently serves as the most fundamental building block for advanced spintronic devices. In 1995, insertion of a thin insulator as the spacer layer (i.e., as the tunnel barrier) resulted in a much higher read-out signal through the effect of TMR (tunneling magnetoresistance)[29], which continued to be further optimized to reach 604% at room temperature in 2008[30]. Combined with the write mechanism of spin-transfer-torque (STT), theoretically predicted in 1996[31,32] and observed in the experiments of switching the magnetization direction[33] and inducing domain-wall motion[34] or high-frequency oscillation[35], both the spin valve and MTJ structures (especially, MTJs employing the crystalline MgO tunnel barrier[36,37]) have gained great attention in the field. The recent discovery of the perpendicular magnetic anisotropy (PMA) in various heterostructure thin films and interfaces offered a new opportunity for low-power data storage applications[38–40]. The reviving interest in the Hall effect[41] will link the spin Hall effect (SHE) with measurable quantities such as spin accumulation, aiming at driving magnetization dynamics more efficiently for the development of energy-efficient spintronic devices.

The ability of spintronics to perform previously impossible experiments and test fundamental theories of magnetism has recently been made possible through the use of 2D materials. Layered materials have, indeed, existed for eons (i.e., studied scientifically for more than 150 years[42]). However, only recently have researchers begun to realize the true potential of these layered materials for advanced technological applications. Each layered material, when thinned down to its physical limits, exhibits novel properties different from its bulk counterpart. Therefore, these materials are specifically referred to as "2D materials". The most widely studied 2D material is graphene[43], which is an atomically-thin sheet of carbon atoms with a bonding length of 1.42 Å. Pristine graphene behaves as a zero-bandgap semimetal,

[1]Department of Electrical and Computer Engineering, The University of Texas at San Antonio, San Antonio, TX 78249, USA. ✉email: ethan.ahn@utsa.edu

npj nature partner journals

constituting an important class of carbon allotropes exhibiting unique 2D hexagonal structures. Readers interested in recent advances and a broad range of commercial applications of graphene will find the 2019 review article by Kong et al.[44] an excellent resource. A wide spectrum of other 2D inorganic materials is also experiencing numerous research efforts owing to their versatile crystal structures and physical properties, including insulators (e.g., hexagonal boron nitride, h-BN)[45], semiconductors (e.g., transition metal dichalcogenides such as MoS_2)[46,47], superconductors (e.g., $NbSe_2$)[48], and even magnets (e.g., CrI_3)[49].

This review discusses 2D materials in the context of spintronic device technologies, focusing on their progress, prospects, and challenges. We examine how 2D materials can be interfaced with other classes of materials, including ferromagnets (FMs), to enable, develop, and advance spintronic devices. Spin-dependent properties of 2D materials are also highlighted in terms of spin-orbit and spin-valley couplings. Major challenges and future perspectives for the development of spintronic devices using 2D materials are finally discussed.

GRAPHENE FOR SPIN LOGIC

Among various device concepts for beyond-CMOS logic switches[50], spin-based, non-volatile digital logic[51–58] (Fig. 1a) has attained much attention because it offers the functionality at lower power consumption by building logic units with magnetic elements. In particular, the proposal of all-spin logic (ASL) switch[51] has been considered to be quite attractive for a future computing paradigm due to its potential for extremely low-power consumption[59,60]. This is because, in the ASL, nonlocal spin currents[61–63] are used to selectively route communication signals between the input and output magnets without spin-to-charge conversion (Fig. 1b). However, a major challenge has been to develop a suitable spin transport channel material that simultaneously achieves a high spin injection efficiency (from FM to the channel material) and a long-distance spin propagation (within the channel material). Graphene, a hexagonal 2D arrangement of sp^2-bonded carbon atoms, may be uniquely suited for this purpose due to its (1) relatively long spin diffusion length and lifetime (theoretically predicted, and experimentally being examined) and (2) ability to be readily interfaced with other classes of materials, including FMs.

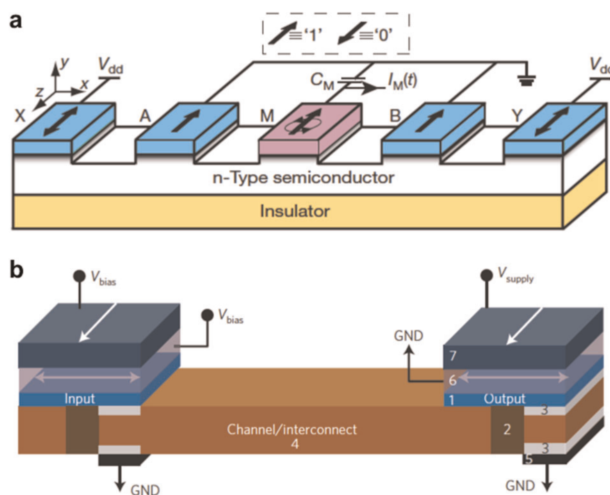

Fig. 1 Spin logic devices. a Reconfigurable spintronic logic gate[52], showing a NAND operation between *X* and *Y*. A and B are chosen to be "1" for NAND, but one may adjust the magnetization alignments of A and B to set different logic operations. The output is given by a transient current response, $I_M(t)$, whose amplitude is proportional to the spin accumulation in the semiconductor. A transient current is allowed to pass through the probing contact (*M*) during the magnetization rotation, where the potential level inside *M* is perturbed and the capacitor (C_M) tries to restore the new steady-state condition ($I_M = 0$). In order to write the magnetization directions of the contacts in cascaded logic gates, $I_M(t)$ needs to be converted to a binary voltage signal. V_{dd} is the supply voltage. **b** All-spin logic (ASL) switch[51], where nonlocal pure spin currents transport information between nanomagnets (i.e., digital spin capacitors). The state of the output magnet is determined by two spin torques with the information provided from the input magnet: one relatively large torque is exerted by the application of V_{supply} and the other small torque is exerted by the application of V_{bias} (for "receive" and "send" respectively, in the cascaded logic gates). 1: magnetic free layer, 2: isolation layer (electrostatic barriers or insulation layers), 3: tunneling layer (oxides or Schottky barriers), 4: spin-coherent channel, 5: contact, 6: spacer layer, and 7: magnetic fixed layer. Image of **a** reprinted by permission from Springer Nature: ref. [52], Copyright 2007. Image of **b** reprinted by permission from Springer Nature: ref. [51], Copyright 2010.

Spin injection, transport, and relaxation in graphene

Graphene exhibits properties attractive for spintronic device applications[64,65]. It has intrinsically low spin-orbit coupling (SOC); at the Γ point, the spin-orbit splitting of the σ band is calculated to be as low as 8.8 meV[66,67]. This can lead to spin coherence maintained over the long distance. Graphene also features ultra-high carrier mobility of reaching up to more than 200,000 $cm^2 V^{-1} s^{-1}$ in a suspended device structure[68], which can enhance the diffusive transport of spin. Advances in spin injection into graphene, experimental determination of spin transport properties of graphene, and understanding of the spin relaxation mechanism in graphene will ultimately contribute to the development of the spin logic device adopting graphene as a spin transport channel.

Nonlocal spin valve (NLSV)

The NLSV[63,69] is the most commonly used device geometry for generating pure spin currents. When the spin-polarized current is injected from a FM contact into a channel material, the accumulated spin in the vicinity of the FM/channel interface can diffuse laterally, thus forming a pure spin current. This nonlocal spin current constitutes a key part of the ASL switch, enabling the input logic bit to control the state of the corresponding output through the spin-torque mechanism[70]. Moreover, the spin-dependent properties of graphene have been quantitatively understood by measuring the NLSV built upon graphene[71], consisting of two FM (one as a spin injector and the other as a spin detector) and two corresponding nonmagnetic (NM) metallic contact electrodes integrated on top of the graphene spin transport channel (Fig. 2a). In this graphene-based NLSV structure, sweeping the in-plane magnetic field (H_y) allows both parallel and antiparallel configurations of two FM electrodes with different shape anisotropy, thus resulting in the nonlocal spin signal, $\Delta R_{NL} = \Delta V_{NL}/I$ (Fig. 2b). ΔV_{NL} is the nonlocal voltage difference between parallel and antiparallel states of two FMs measured at the FM detector side ($\Delta V_{NL} = V_{NL}^{P} - V_{NL}^{AP}$) and I is the injection current through the FM injector. This four-terminal measurement geometry is called nonlocal because the voltage is measured "outside" the (charge) current loop. One key advantage of this NLSV geometry is that background noise signals from charge currents are greatly reduced due to the absence of net charge flow. Importantly, the nonlocal spin signal will only be dependent on the relative orientation of the FM detector's spin with respect to those accumulated at the FM injector. Thus, it is possible that ΔR_{NL} is measured by varying the injector and detector separation (*L*) because the magnitude of spin accumulation will decay as it diffuses away from the injection point, with a characteristic length known as spin diffusion length (L_D). This is described by the

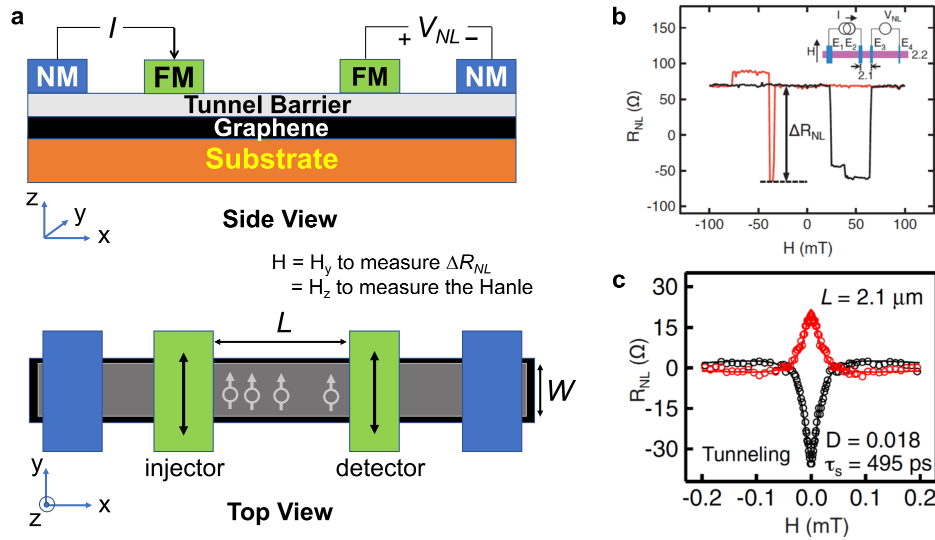

Fig. 2 Graphene nonlocal spin valve. a Schematics of the graphene nonlocal spin valve (NLSV), showing both the side and top view images with graphene as a spin transport channel. FM and NM represent ferromagnetic and nonmagnetic metals, respectively. The spin transport properties of graphene can be determined by measuring the difference in nonlocal resistances between parallel and antiparallel states of two FMs (ΔR_{NL}) with varying the injector and detector separation (L), or measuring the Hanle curve by applying an out-of-plane (H_z) magnetic field to induce a spin precession. **b** The nonlocal resistance measurement with the graphene NLSV that has the FM contact separation distance (L) of 2.1 µm and the monolayer graphene channel width (W) of 2.2 µm[82]. Co (Cobalt) is used in this work to represent the four contact electrodes (E1 through E4) with the MgO/TiO_2 bilayer tunnel barrier inserted at the Co and graphene interface. The black (red) curve shows the nonlocal resistance as the magnetic field (H) is swept in the $+y$ ($-y$) direction. ΔR_{NL} will exponentially decay with the increasing separation distance. **c** The Hanle spin precession curve for the same device structure, showing red (black) circles for parallel (antiparallel) alignment of the FM electrodes[82]. The spin diffusion constant (D) and lifetime (τ_s) are extracted as the fitting parameters to Eq. 2. Images of **b** and **c** reprinted with permission from ref. [82] Copyright 2010 by the American Physical Society.

equation below (Eq. 1)[69].

$$\Delta R_{NL} = \frac{\eta^2 L_D}{2W\sigma} exp(-L/L_D) \tag{1}$$

In this equation, σ is the conductivity, W is the width of the graphene channel, and L is the contact spacing. η is the spin injection efficiency, often represented by the spin polarization of the injection current $\left(\frac{I_{majority}-I_{minority}}{I_{majority}+I_{minority}}\right)$, where majority (minority) means the spin direction parallel (antiparallel) to that of the FM injector. Fundamentally, η is directly related to the spin polarization of the FM contact electrode $\left(\frac{DOS_{majority}-DOS_{minority}}{DOS_{majority}+DOS_{minority}}\right)$, where DOS is the density of states at the Fermi level, modulated by any presence of spin-flip scattering at the FM/channel interface. It is noted that above definitions, including Eq. 1 and spin polarization of FM electrodes, are only valid for the case of tunnel barrier contacts.

The graphene-based NLSV also enables a precise characterization of spin precession signals in graphene by applying an out-of-plane magnetic field and then measuring the nonlocal resistance (R_{NL}) as a function of the magnetic field strength (the Hanle effect[61,72]) (Fig. 2c). Many experimental studies on the spin transport parameters of graphene have been performed by conducting the Hanle measurement in the nonlocal geometry because the Hanle spin precession curve is a strong indicator of pure spin currents in graphene. The Hanle measurement offers a more reliable way to study spin transport in graphene because the approach based on Eq. 1, requiring the NLSV device structure to be repeatedly fabricated for varying the separation distance, often encounters a significant challenge in reproducing the same FM/graphene tunnel contacts[73]. The spin lifetime (τ_s) and the spin diffusion constant (D_s) can be extracted as fitting parameters to the following equation (Eq. 2)[61,72,74].

$$R_{NL} \propto \pm \int_0^\infty \frac{1}{\sqrt{4\pi D_s t}} exp\left(-\frac{L^2}{4D_s t}\right) \cos(\omega t) exp\left(-\frac{t}{\tau_s}\right) dt \tag{2}$$

Here, the +(-) sign is for the parallel (antiparallel) magnetization state, and ω is given by $g\mu_B B_\perp/\hbar$, where g is the Landé factor ($g = 2.0023$) and $\hbar$ is the reduced Planck's constant. Once τ_s and D_s are determined from the Hanle measurement and analysis, the corresponding spin diffusion length (L_D) can be calculated by $L_D = (D_s\tau_s)^{1/2}$.

Spin injection into graphene

The difficulty in utilizing the conventional semiconductor materials (e.g., silicon) for emerging spin logic applications arises from the facts that (1) their spin transport properties tend to degrade with the decreasing film thickness (i.e., poor scalability)[75], and (2) the spin injection from a FM metal contact into a semiconducting channel material has been a great challenge due to a fundamental conductivity (or mode) mismatch problem[76]. Noticeably, a recent experimental study has reported that graphene can transport spin signals over a relatively long distance of up to 30.5 µm[77] (this distance can be increased even up to 90 µm using carrier drift[78]). If spin injection from the FM electrode into the graphene channel can be made with a high injection efficiency, the use of graphene as a spin transport channel may be considered as a practically viable route for the development of emerging spin logic devices.

Since the first demonstration of spin transport in graphene at room temperature in 2007[71], spin injection efficiency into graphene has been continuously improved. Inserting a thin tunnel barrier (TB) at the FM/graphene interface has been widely used to mitigate the conductivity mismatch problem and, thus, increase the spin injection efficiency into the graphene layer. Injection efficiencies of up to ~30% have been experimentally demonstrated using a variety of TB materials such as TiO_2[79,80], MgO[81], TiO_2-seeded MgO[82,83], h-BN[84], and Al_2O_3[85–87] (Table 1). More recently, even the fluorinated graphene was used as a homoepitaxial TB material to the graphene channel, achieving the tunneling spin polarization of up to 60%[88]. It is worth, however, noting that these TB-based approaches may still experience the

Table 1. Summary of spin injection and transport properties of graphene.

FM/TB	η	Prep. method		Sub.	I.	Graphene mobility (cm^2/Vs)	Spin transport Parameters			Mecha.	Ref.
		TB	Gr.				L_D (μm)	τ_S (ns)	D_S (m^2/s)		
Co/TiO_2	6%[79]	0.4 nm Ti, oxidation	Exfoliation	h-BN	N	40,000	4.5	0.39	0.052	EY + DP	92
		0.5 nm Ti, oxidation	Exfoliation	SiO_2	N	2,500	0.75	0.075	0.0075	–	79
		0.4 nm Ti, oxidation	CVD	SiO_2	Y	2,000	6	1.2	0.026	EY + DP	80
Co/MgO	30%[82]	1 nm MgO MBE	Exfoliation	h-BN	Y	20,000	10	2	0.05	–	93
		1.2 nm MgO MBE	Exfoliation	h-BN	Y	20,000	30.5	12.6	0.074	–	77
		–	Exfoliation	SiO_2	N	2,000	0.7	0.135	0.0032	DP	100
		<3 nm MgO MBE	Exfoliation	SiO_2	N	3,000	–	<0.1	–	DP	81
		0.8 nm MgO MBE	Exfoliation	SiO_2	Y	2,000	2.4	0.447	0.013	EY	83
		0.8 nm MgO MBE	Exfoliation	SiO_2	Y	–	3	0.495	0.018	–	82
Co/Al_2O_3	10%[78]	1 nm Al_2O_3 Evaporation	Exfoliation	Suspend	N	100,000	2	0.2	0.02	DP	87
		0.6 nm Al, Oxidation	Exfoliation	SiO_2	N	2,000	2	0.17	0.02	–	71
		0.6 nm Al, Oxidation	Exfoliation	SiO_2	N	3,500	2	0.145	0.027	EY	86
Py/Al_2O_3	6%	ALD at 100 °C	Exfoliation	SiO_2	N	2,500	4.2	0.175	0.1	–	85
Py/h-BN	–	0.34nm h-BN	Exfoliation	h-BN	N	2,300	1.1	0.055	0.034	–	84
Py/f-Gr.	63%	Fluorinated Gr. (with XeF_2)	CVD	SiO_2	N	–	1.5	0.2	0.012	–	88

Spin transport parameters of graphene (L_D, τ_S, D_S) are experimentally measured at room temperature by using the four-terminal NLSV device geometry. Most works directly measure two of these parameters via the Hanle effect[61,72] (or the separation distance method[69]) and then calculate the other parameter based on the fundamental relation of $L_D = (\tau_S D_S)^{1/2}$. Spin injection efficiency (η) is typically estimated by the spin polarization of the tunneling current (Eq. 1). FM/TB indicates the type of ferromagnetic (FM) contact and tunnel barrier (TB) materials. Prep. method lists how each work prepares the tunnel barrier (TB) and graphene (Gr.) channel materials. Most works used the mechanical exfoliation technique to integrate graphene into the NLSV device. The substrate type (Sub.) is also shown for each work, implying that the use of h-BN tends to enhance spin transport characteristics due to increase in graphene mobility. The effect of graphene interface treatment (see column I. for whether each study has employed any interface engineering techniques; Y for yes and N for no) on spin transport properties is very noticeable, thus suggesting any further systematic study to elucidate the extrinsic origin of varying spin transport parameters in graphene. Any proposed mechanism for spin relaxation is also shown in column Mecha.

above-mentioned issue of lacking the ability to reproduce the same FM/graphene tunnel contacts. More studies will need to be conducted to better quantify the spin polarization and understand what extrinsic factors (e.g., bias-dependence) impact the experimental measurements[89–91].

Enhancing the spin injection efficiency is very important from the power perspective; the lower spin injection efficiency means that more charge currents would be pumped into the graphene channel to form a sufficiently large spin accumulation that can switch the corresponding output magnet. Most experimental studies have used Eq. 1 to estimate the spin injection efficiency parameter (η) by performing the NLSV experiment. A fundamental limitation of this approach is that the measurement accuracy of η will strongly depend on measurements of other parameters in the equation. Most notably, the spin diffusion length (L_D) of graphene seems to largely vary among different studies (Table 1). Without any further optimization or new development of the graphene integration process (otherwise, the device integration process may entail exposure of graphene surfaces to organic and/or inorganic contaminants), this may impose a significant challenge in making the reliable measurement of spin transport parameters, consequently limiting the accuracy of the spin injection efficiency calculation. The next section below discusses the topic of spin transport and relaxation in the graphene spin transport channel.

Spin transport and relaxation in graphene

Table 1 summarizes the experimental measurements of graphene's spin transport properties, with various substrate materials, FM contact electrodes, TBs, and preparation methods. Taking a close look at this table will provide several useful insights into the spin transport phenomena in graphene.

First, as seen in Fig. 3a, the use of h-BN as a substrate for graphene tends to increase the spin diffusion constant (D_s) of graphene, thus enhancing the long-distance propagation of spin signals in the graphene channel layer[77,92,93]. This is due to the high carrier mobility in graphene, having h-BN as the substrate; experiments have already shown that the measured Hall mobilities of graphene devices fabricated on the h-BN substrates are even comparable to the best-reported values of the suspended graphene devices[94]. By the Einstein relation, the high carrier mobility leads to a high diffusion constant for charge carriers. Consequently, the diffusion constant increases for spin because spin current is carried by charged particles in the NLSV. The graphene/h-BN or other 2D van der Waals (vdW) heterostructures[95–97] may be considered as the high-performance spin transport channel.

The phenomenon of spin relaxation in graphene can be understood by examining Table 1 on how the spin transport parameters change with other independent variables. For example, investigation of a possible relation between spin lifetime (τ_s) and charge carrier mobility (μ) has been a topic of great scientific interest because it would help reveal the relevant spin scattering mechanism. A linear dependence of τ_s on μ is suggestive of the Elliott–Yafet (E.–Y.) spin scattering mechanism[98], while the inverse relation ($\tau_s \sim 1/\mu$) indicates the dominance of the Dyakonov–Perel (D.–P.) mechanism[99]. A previous study on spin relaxation in bilayer graphene films on SiO_2[100] observed a clear inverse dependence of τ_s on μ, suggesting the D.–P. model as a dominant mechanism that correlates the spin and charge transports; spin phases are randomized between collisions as electrons precess with different frequencies depending on their momenta. However, as summarized in Table 1, it is possible that both the E.–Y. and D.–P. mechanisms are simultaneously relevant[80,92], or the E.–Y. scattering, where the precession frequency is conserved between collisions and the phase loss occurs only in the short time during collision, becomes a major causative factor for spin relaxation in graphene[83].

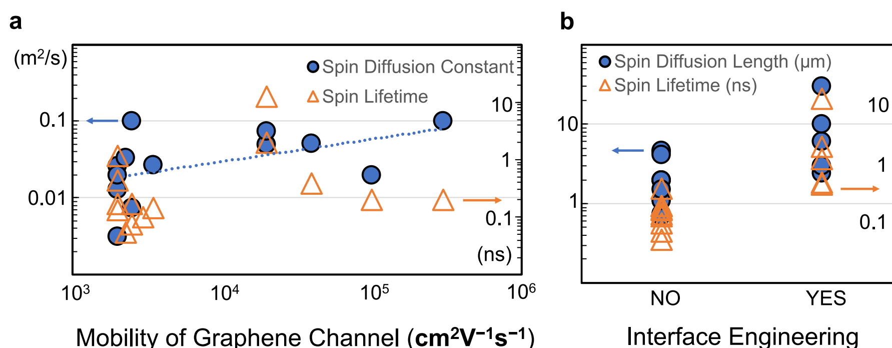

Fig. 3 Spin transport properties of graphene. a Impact of graphene mobility on the spin diffusion constant (solid circles, left axis in the unit of m^2/s) and lifetime (empty triangles, right axis in the unit of nanoseconds) values. It is seen that spin diffusion constant tends to increase when the graphene spin transport channel is prepared to be of high quality (high mobility). The dotted line is the fitted curve to the data points obtained from various studies in Table 1. Unlikely, the spin lifetime exhibits almost the negligible dependence on the graphene channel's mobility. **b** Impact of interface engineering on the spin diffusion length (solid circles, left axis in the unit of μm) and lifetime (empty triangles, right axis in the unit of nanoseconds). Both the spin diffusion length and lifetime values are significantly enhanced upon the various interface engineering techniques used, such as annealing of the graphene surface[80], the use of a large h-BN flake to prevent diffusion of solvents during the graphene transfer process[77], and angle evaporation of the tunnel barrier oxides on the graphene surface[82].

Another piece of information available from Table 1 is that τ_s and L_D values largely vary among different studies using the same TB material. This indicates that the microscopic origin for such a large discrepancy among various studies on spin transport in graphene could be best understood by examining the experimental details and setups of each study. One important conclusion from such deep analyses is that some special treatment of the graphene interface has resulted in significant improvement of the spin transport characteristics in graphene (Fig. 3b). For example, the thermal annealing technique (@ 400 °C in Ar/H_2) that has been applied after transferring the CVD (chemical vapor deposition)-grown graphene layer yielded significantly higher τ_s and L_D values of 1.2 ns and 6 μm, respectively[80], as compared with other similar studies using the SiO_2 substrate[71,79,81–83,85,86,100]. Furthermore, the highest values of τ_s and L_D ever reported to date (τ_s of 12.6 ns and L_D of 30.5 μm)[77] were obtained by synergistically combining the two interfacial engineering techniques: (1) reversing the conventional NLSV fabrication order (i.e., from graphene first and then tunnel barrier, to tunnel barrier first and then graphene[93]), and (2) reducing the contamination of the FM/TB/graphene interfaces[77]. More recently, a few other works also reported spin transport in the CVD-grown graphene over the long distance of larger than 30 μm[101,102]. It is noted that τ_s and L_D values, exceeding 100 ns and 100 μm, respectively, have once been reported for epitaxial graphene on SiC[103]. However, this experiment was conducted in the local, two-terminal geometry, limiting the measurement accuracy. Therefore, further research will need to be conducted to study if any particular interface within the FM/TB/graphene tunnel junction is responsible for significant spin dephasing or flipping. This will ultimately help suggest practical solutions to achieve the excellent spin propagation in graphene approaching the theoretically predicted values (e.g., $\tau_s \sim$ a few μs)[104–106].

Inducing magnetic moments in graphene

Fundamentally, pristine graphene is strongly diamagnetic as it does not consist of *d* or *f* electrons. However, any possibility of inducing magnetic moments in graphene has been the great scientific and technological interest in the field. In particular, from the perspective of advancing the spin logic device, the existence of atomically-thin permanent magnets would mean that conventional FM thin films can be replaced by a highly scalable, novel spin injector (or detector) material. This is important because conventional FM thin films with thicknesses of less than 200 nm typically experience noticeable changes in their magnetic properties such as magnetic anisotropy[107]. It is also known that for the magnetic thin films even in the monolayer or few-layer range, the magnetic ordering (Curie) temperature is strongly affected by a variety of topological effects such as vacancies, substrate roughness and atomic intermixing, and incomplete crystal structures[108].

Besides the recent discovery of 2D magnets[49], the graphene itself has experienced significant research efforts to induce magnetic moments by extrinsic factors. Introducing light adatoms (point defects) such as hydrogen (H)[109,110] or fluorine (F)[111,112] has been the most popular approach to inducing localized magnetic moments in graphene. This is possible because the hydrogen or fluorine can be reversibly chemisorbed on graphene[113,114], thus creating a sublattice imbalance by removing one p_z orbital from the π band. According to the Lieb's theorem[115], the single hydrogen adatom can induce a quasi-localized state in graphene with magnetic moment of $1\mu_B$. A recent theoretical study even predicted that graphene in the form of quantum dots (e.g., zigzag graphene nanoflakes) can exhibit strong edge magnetism at room temperature due to the presence of localized edge states[116]. Despite the fact that magnetic moments in graphene have been experimentally observed by adopting the various techniques of SQUID (superconducting quantum interference device, using the Josephson junction to characterize the dependence of supercurrents on magnetic fields)[111], MFM (magnetic force microscopy)[117], and nonlocal[110] or local[112] spin transport measurements, making graphene permanently magnetic (beyond just inducing the *localized* magnetic moments) still remains a great challenge.

2D MATERIALS FOR MTJ AND TRANSISTORS

This section reviews recent experimental efforts to integrate 2D materials in other equally-important classes of spintronic devices—namely, MTJs and spin transistors. Owing to the unique ability of 2D materials to gain the highly homogenous atomic control over their thickness, researchers began to consider them as a critical element for these emerging spintronic devices. Many perspectives are being opened up in exploring the vast amount of 2D material family and their heterostructures, aiming to achieve specific spin device properties.

MTJs

The MTJ is a modern spintronic device that can be used for processing the bit information stored in the nanomagnet[29].

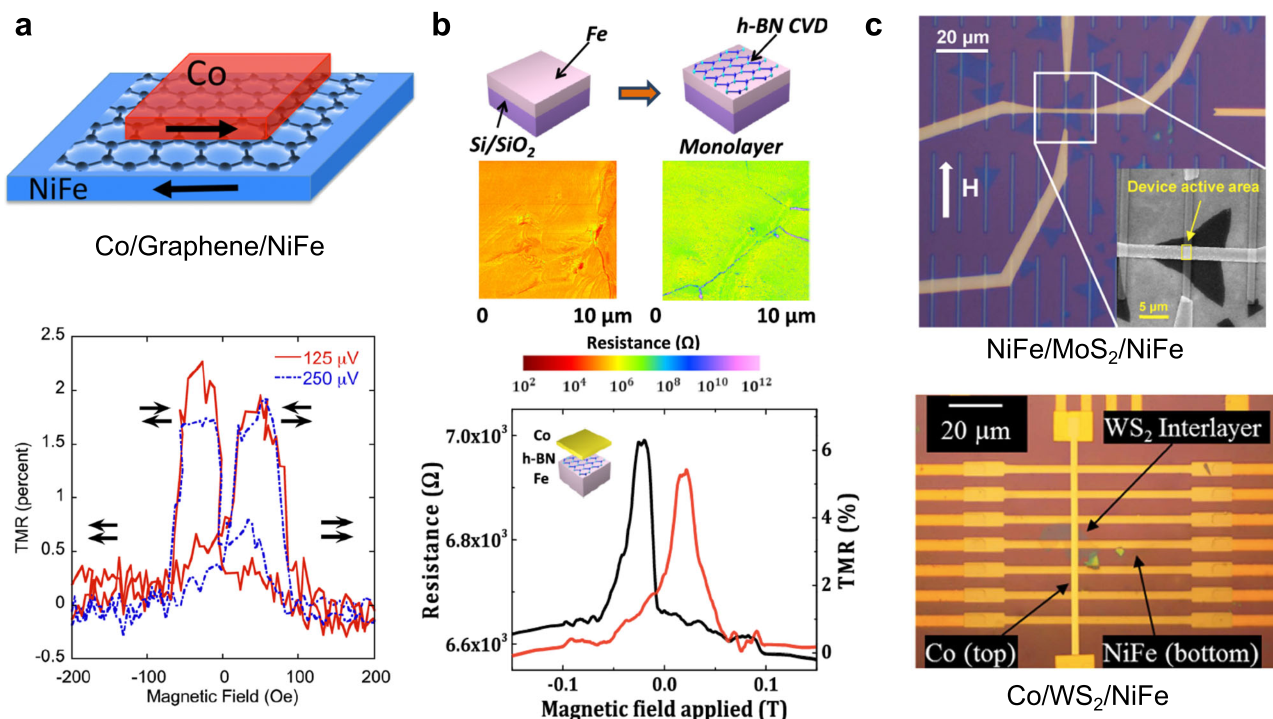

Fig. 4 2D Materials for MTJ. a The graphene-inserted magnetic tunnel junction (MTJ) device (top), and measured TMR characteristics (bottom) at temperature of 4 K and with low bias voltages (125 and 250 μV) applied[124]. The CVD-grown graphene is transferred onto the 20 nm NiFe FM electrode. The arrows in the TMR graph indicate the relative orientation of the NiFe (lower) and Co (higher) FM contacts. **b** The Co/h-BN/Fe MTJ device structure is fabricated by annealing the Fe substrate, then directly growing h-BN on the Fe catalytic substrate via the low-pressure CVD technique (top), and finally depositing the 15 nm Co top electrode by evaporation[128]. The conductive AFM (atomic force microscope) measurement yields the resistance values of 10^5 Ω for the Fe substrate and 10^7 Ω for the monolayer h-BN/Fe stack. The relatively high TMR ratio of about 6% is reported in this work (bottom), arising from suppression of the FM electrode oxidation due to direct CVD growth of h-BN on top of the FM electrode. **c** Monolayer TMD is used as the spacer layer in the ferromagnetic sandwich structure to result in the spin valve effect[132,134]. The NiFe/MoS_2/NiFe device with monolayer MoS_2 grown by CVD and transferred by the wet process (top)[132] and the Co/WS_2/NiFe device with the exfoliated single-layer WS_2 (bottom)[134] exhibit the magnetoresistance ratios of up to 0.73% and 0.47% at low temperatures, respectively. Image of **a** reprinted with permission from ref. [124]. Copyright 2012 American Chemical Society. Image of **b** used from AIP Publishing with permission under a CC-BY 3.0[128]. Image of **c** (top) reprinted with permission from ref. [132]. Copyright 2015 American Chemical Society. Image of **c** (bottom) used from Springer Nature with permission under a CC-BY 4.0[134].

The active area of MTJ typically consists of two FM electrodes with a thin insulating barrier sandwiched between them. The spacer layer is extremely thin (e.g., MgO in the nanometer or sub-nanometer range), leading electrons to tunnel through it. The MTJ has enabled the development of STT-MRAM (spin-transfer-torque magnetic random-access memory) for high-performance data storage and computing applications[118–120], where spin-polarized currents exert a STT to change the magnetization direction of a nanomagnet. With its close-to-market position towards commercialization (e.g., in 2019, Everspin announced the sampling of 1 Gb STT-MRAM chips), STT-MRAM now becomes the most promising candidate to replace SRAM to bring the emerging paradigm of non-volatile embedded memory. However, further improvement of device performances and bit-cell scaling are still the great challenges due to issues related to controlling the TB and interfaces, the thermal stability, and the robustness[118]. In this context, 2D materials possess the potential to address some or all of these issues because they offer a precise control of the ultimate thickness while still affording sharp interfaces with other classes of materials. This will allow 2D materials to serve as an atomically-thin spacer layer in MTJ.

Graphene as a tunnel barrier

An early theoretical study on the FM/graphene interface[121] triggered research on harnessing graphene as an atomically-thin spacer layer in MTJ. This was driven by the facts that (1) the in-plane lattice constant of graphene (2.46 Å) matches almost perfectly that of (111) Co or Ni (the lattice mismatch between them is only less than 1.3%), and (2) their electronic band structures in the reciprocal space overlap at the Fermi level only for one spin direction (spin filtering). Indeed, the theoretically predicted TMR ratio of the FM/graphene/FM stack was as high as about 100% owing to the perfect spin filtering effect[37] assumed for the FM/graphene interface. Although Mohiuddin et al. demonstrated the first experimental work, adopting the exfoliated monolayer graphene in a Permalloy (NiFe)-based MTJ structure[122], the reported TMR ratio was only 0.4%. Many other follow-up studies on the similar device stack, either using monolayer, bilayer, or few-layer graphene or other 2D materials (e.g., MoS_2, WS_2, h-BN), also produced the TMR ratios of less than a few percent[123,124]. For example, Fig. 4a shows the magnetic hysteresis with TMR of about 2% measured with the Co/graphene/NiFe structure[124]. This is mainly due to the integration difficulties in inserting 2D materials between oxidation-prone FM metals; unlike the conventional in situ physical vapor deposition (PVD) process that fabricates the whole MTJ stack without breaking the vacuum, most of these previous works on FM/2D material/FM made the bottom FM electrode exposed to air during the exfoliation or transfer of 2D materials.

The existing strategic effort to prevent oxidation during the fabrication of a graphene-inserted MTJ structure falls into three major categories: inserting a thin buffer layer, the flip-transfer

method, and the use of FM oxides. An example of the first category was to insert a thin noble metallic layer (e.g., Au) at the FM/graphene interface, as shown in the early work of fabricating the NiFe/graphene/Au/NiFe stack (from top to bottom) with the graphene flakes exfoliated onto the Au-coated NiFe electrode[122]. The flip-transfer method employed more complicated process steps of exfoliating graphene on the substrate coated by the LOR (lift-off resist)/PSS (poly (4-styrenesulfonic acid)) bi-layer, depositing the patterned NiFe electrode, separating the NiFe/graphene/LOR stack from the substrate by dissolving the PSS layer in water, and flipping it onto another SiO_2/Si substrate[125]. However, in both the first and second approaches, the obtained TMR ratios were still limited to only about 5%. This was attributed to reduced spin polarization due to the inserted 2 nm-thick Au layer[122] and the antiferromagnetic coupling between FM electrodes[125], respectively. In 2014, Li et al. used a FM half-metal oxide layer of $LaSrMnO_3$ (LSMO) to replace one of the conventional FM metal electrodes, leading to the MTJ stack of Co/graphene/LSMO[126]. Although LSMO is known to exhibit a very high spin polarization (about 95%), this third approach also produced negligibly small enhancement in the TMR ratio, due to contamination of the LSMO interface during the graphene transfer process.

Other 2D materials as a tunnel barrier

h-BN, a wide-bandgap 2D dielectric, can possibly better serve as a TB in MTJ due to its intrinsic insulating nature (bandgap energy, $E_g \sim 6$ eV). Several recent works studied the FM/h-BN/FM structures with h-BN thin films prepared by wet-transfer[127] or direct CVD growth onto the FM electrode[128], yielding the TMR ratios of up to 6% (Fig. 4b). The MBE (molecular beam epitaxy) technique also enabled the direct growth of h-BN onto the FM layer[129], thus providing an alternative pathway to better tailoring the FM/2D material interface and ultimately creating the MTJ structure having the atomically-thin, robust TB. Despite these promising early results on the direct growth of h-BN on FM[128,129], it is noted that both CVD and MBE growth of monolayer or few-layer h-BN crystals would require in-depth investigation of the parameter space for the specific FM substrate. For example, whereas graphene has already been routinely synthesized by CVD on FM catalysts such as polycrystalline Nickel (Ni), the CVD parameter space has only recently been carefully tuned (e.g., lowing the temperature down to about 450 °C) to ensure the monolayer growth of graphene on Ni[130,131].

In 2015, Wang et al. introduced the CVD-grown monolayer TMD (MoS_2) in MTJ[132] (Fig. 4c), by using the Au-coated NiFe electrode to minimize the same oxidation issue already encountered with graphene and h-BN. In this work, the insertion of Au still led to degradation of spin polarization in MTJ, thus producing only a marginal increase in the TMR ratio (from 0.4% to 0.7%). The technique of using the FM oxides was also employed to integrate MoS_2 with Fe_3O_4 electrodes[133], but the spin signal still remained far from expectations (TMR ~0.2%). A more recent study demonstrating the MTJ device with exfoliated WS_2 flakes (Fig. 4c) also resulted in a poor TMR ratio of 0.47% due to the oxidation of the bottom FM electrode[134]. Collectively, the use of TMD materials in MTJ seems still at early stage as compared with graphene and h-BN, requiring more advanced studies in optimizing the MTJ integration process with TMD materials.

Spin transistors

Most spintronic devices discussed so far are passive in the sense that they are not capable of amplifying an electrical signal. An active spintronic device, if successfully implemented, can find it useful in signal processing, logic circuits, etc. A transistor is the three-terminal (neglecting the body effect) active device where the electrical current flow between two terminals is modulated by a voltage (or a current) applied to the third terminal. Inspired by the seminal proposal of the Datta and Das spin modulator[135], many studies have been devoted to electrical control of the spin current, which is key to implementing an emerging device concept of spin transistor[136,137]. In spin transistor, owing to the Rashba spin-orbit interaction (i.e., generation of an *effective* magnetic field by an electric field applied to the gate terminal), the spin injected from the source FM contact travels towards the drain FM contact via Larmor precession. Typically, spin transistor is normally ON (i.e., depletion mode) because no precession at zero gate voltage leads to the spin direction parallel to the drain FM. Varying the gate voltage can then alter the spin precession angle to result in a periodic modulation of the source-to-drain current. Although spin transistor promises performances of higher speed and energy-efficiency than conventional transistors[138], finding the optimal device structure employing the best-suited materials for each element still requires extensive research efforts. This may open up new opportunities for 2D materials and vdW heterostructures due to their versatile crystal structures and functionalities.

TMD/graphene heterostructures as a spin channel

Yan et al. investigated the vdW heterostructure of graphene/MoS_2 as a novel spin transport channel[139]. This study aimed to synergistically combine the unique spin-related properties of graphene and TMD; graphene allows a long-distance spin transport due to its low SOC[66,67] while TMD's strong SOC, originating from the *d*-orbitals of the heavy metal (the spin-orbit splitting is 148 meV in monolayer MoS_2)[140], holds the potential to effectively manipulate spin. In this work, graphene flakes were first exfoliated onto a highly doped silicon substrate coated with a 300 nm-thick SiO_2. Then, a few-layer MoS_2 flake was transferred by all-dry viscoelastic stamping[141] to create a gate-tunable spin sink. Finally, several FM (Co) electrodes with TiO_2 as the TB were patterned and deposited to complete the NLSV geometry. As shown in Fig. 5a, the central result was the demonstration of tuning the spin current (dictated by the nonlocal resistance measured in the NLSV) by varying the back-gate voltage (V_g) applied to the substrate. For a negative V_g of less than −10 V, the MoS_2's low sheet conductance made the spin current flow well in the adjacent graphene channel. For a positive V_g of higher than 10 V, the MoS_2 sheet conductance increased to absorb much of the spin current from graphene. The authors supported this argument by estimating and comparing the spin resistances of the graphene channel and the MoS_2 spin sink. Despite the lack of direct evidence of a link between the strong SOC and the proposed spin absorption mechanism in few-layer MoS_2, this work featured the electrical manipulation of spin current at relatively high temperatures (up to 200 K) and the well-defined ON and OFF states. The room temperature demonstration of the electrical control of spin current in the similar MoS_2/graphene heterostructure quickly followed up, with a clearer understanding of the spin transport mechanism in such a vdW heterostructure[142]. The great tunability of spin current was rather attributed to the gate tuning of the Schottky barrier at the MoS_2/graphene interface, leading to the modulation of MoS_2's conductivity. For example, at high gate voltages applied, the reduced Schottky barrier and MoS_2's conductivity allowed spin to tunnel into MoS_2, making it dephasing due to the high SOC of the MoS_2 channel.

It is also important to note that graphene, when interfaced with TMD, exhibits a unique spin lifetime anisotropy (SLA) effect. The SLA, defined as the ratio of lifetimes for spins pointing out of the graphene plane to those pointing in the plane, was theoretically predicted to reach values of tens to hundreds in the TMD/graphene heterostructures[143]. This phenomenon was experimentally demonstrated in $MoSe_2$/graphene[144] and WS_2 (or MoS_2)/graphene[145] heterostructures, showing an order of magnitude longer lifetime for out-of-plane spins (i.e., SLA~10). The SLA effect,

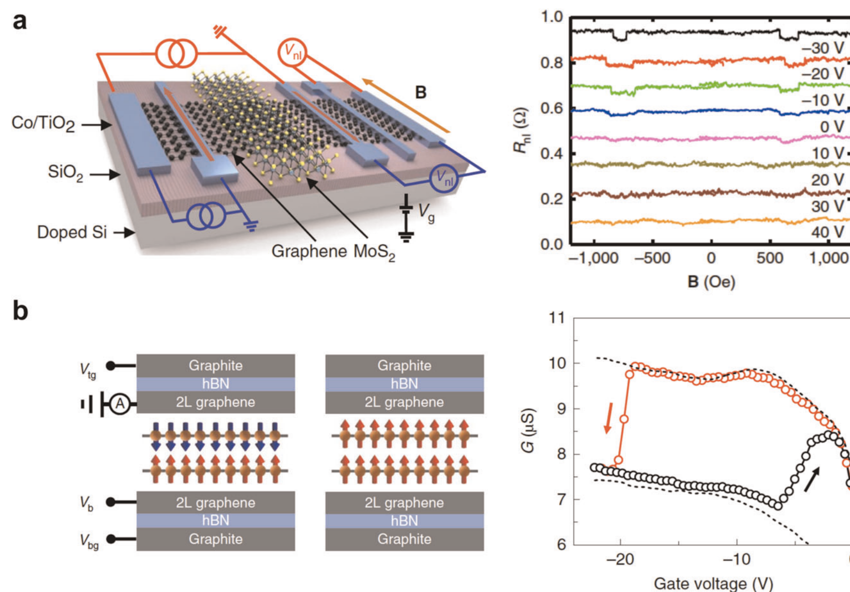

Fig. 5 2D materials for spin transistor. a The device schematic of MoS_2/graphene heterostructure-based spin transistor (left) and measured nonlocal resistances (R_{nl}) with a wide range of gate voltage biases (V_g) applied (right)[139]. For the nonlocal measurement, a DC current of 10 μA is injected into graphene from the Co/TiO_2 tunnel contact electrode. The measured nonlocal voltage (V_{NL}) (and thus, resistance $R_{NL} = V_{NL}/I$) varies with V_g due to the spin current (flowing in graphene) modulation by the MoS_2 spin absorber (sink). **b** The spin tunnel FET (spin TFET) concept is proposed as an alternative way to implement spin transistor (left)[146]. Instead of controlling the spin current in the spin transport channel, the spin TFET harnesses electrical switching of the magnetization configuration (in much the same way as MTJ) to create the transistor output. The recently discovered 2D magnet, bilayer CrI_3, is used as the active switching medium due to its spin-flip transition behavior. The fabricated device offers a large ON/OFF conductance (G) ratio approaching 400% (right). Image of **a** used from Springer Nature with permission under a CC-BY 4.0[139]. Image of **b** reprinted by permission from Springer Nature: ref. [146], Copyright 2019.

while serving as direct evidence of strong spin-valley coupling in the TMD material (this topic will be revisited in a later section), may provide an alternative route for manipulating spin relaxation in 2D material-based spintronic devices.

2D magnets to realize a spin tunnel transistor

A very recent effort to enable spin transistor by 2D materials led to the development of a novel form of spin transistor—namely, spin tunnel field-effect transistor (spin TFET)[146]. In contrast to the originally proposed (Datta and Das) spin transistor concept, relying on the electrical control of spin current in the high SOC channel material, spin TFET is constructed by incorporating the emerging 2D magnetic crystal as the magnetic TB (Fig. 5b). Among many 2D magnetic materials recently discovered[49,147–152], the layered magnetic insulator, CrI_3, exhibits an intriguing thickness-dependent magnetic order; monolayer CrI_3 is a perpendicular FM, whereas bilayer CrI_3 is an antiferromagnet consisting of two FM monolayers with antiparallel magnetic moments. Importantly, under a moderate magnetic field applied (less than 1 T), the bilayer CrI_3 can even be switched to FM through a spin-flip transition. Moreover, one study demonstrated that switching of bilayer CrI_3 between antiferromagnetic and ferromagnetic states can be induced by an electric field[153]. Therefore, in this study, the vertical junction of graphene/CrI_3/graphene was fabricated to examine the electrical switching behavior of CrI_3, interfaced with graphene top (source) and bottom (drain) contacts (Fig. 5b). Alongside the earlier demonstrations of the spin filtering effect in CrI_3, giving rise to the large TMR signal in tunnel junctions[154–156], this work significantly advanced the spin transistor research by presenting an ambipolar transistor behavior with a high ON/OFF ratio approaching 400%. This was achieved by electrically controlling (gate tuning) the magnetization configuration of the 2D magnetic insulator, instead of directly modulating the spin current.

SPIN-ORBIT COUPLING IN 2D MATERIALS

Spin-orbit coupling (SOC) refers to the relativistic phenomenon of exerting a torque on the elementary particle with spin, approaching the nearby atom to "feel" the orbital motion. SOC is responsible for many inspiring physical properties of 2D materials, including the room temperature quantum Hall effect (quantization of Hall resistance under a large magnetic field) observed in monolayer graphene[157,158]. From the technological point of view, SOC is of great importance because it provides an effective means of generating a pure spin current even in nonmagnetic materials via the SHE (spin accumulation with no Hall voltage)[159]. Indeed, the room temperature SHE was recently observed in the graphene/MoS_2 vdW heterostructure (Fig. 6a)[160], which is best attributed to the valley-Zeeman type of SOC imprinted from TMD to graphene (i.e., the proximity-induced enhancement of SOC in graphene due to a weak hybridization with the heavy atoms in TMD)[161]. The charge-to-spin conversion can also occur in the graphene/TMD heterostructure via the Rashba-Edelstein effect (due to the broken out-of-plane symmetry)[162], which was recently demonstrated with graphene in conjunction with the monolayer WS_2[163]. The SOC-induced pure spin current is currently being widely researched in the field, for the purpose of developing the advanced spin-orbit torque (SOT) devices such as SOT-MRAM[164] and SHO (spin Hall oscillator)[165]. Most early experimental studies on these devices interfaced FM with a heavy metal of large SOC (e.g., Ta, Pt) to effectively induce magnetization switching or oscillation. However, the state-of-the-art SHA (spin Hall angle, θ_{SH}, an important metric for charge current-to-spin current conversion efficiency) of heavy metals is limited to θ_{SH} of less than 0.1, with greatly varying values among different studies[166]. This imposes a significant challenge in developing energy-efficient, high-performance spintronic devices because the large SHA value means that a large amount of charge currents will still need to be supplied. This may offset the benefits of using spin for electronics. With the giant SOC-induced spin splitting already reported for

Published in partnership with FCT NOVA with the support of E-MRS

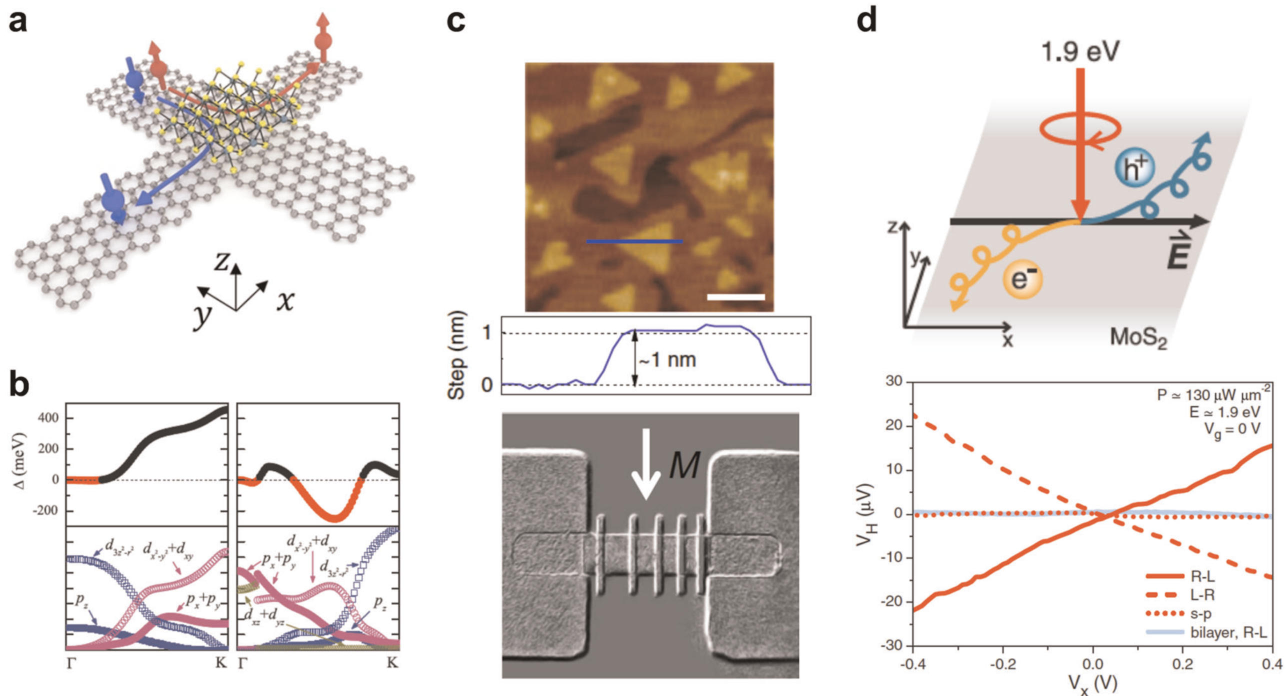

Fig. 6 Spin-orbit coupling in 2D materials. a The room-temperature spin Hall effect observed in graphene, in the proximity of high spin-orbit coupling 2D material (MoS_2)[160]. A charge current applied along the graphene/MoS_2 stripe (*y* axis) results in a spin current with out-of-plane (*z* axis) spin polarization in the graphene channel along the *x* axis. **b** Spin splitting (Δ in the unit of meV) of the WSe_2 monolayer system, shown in the momentum space along the Γ-K line for the uppermost valence band (left) and the lowermost conduction band (right)[140]. The bottom panels show contributions of orbitals for Se (p_z, $p_x + p_y$) and *W* ($d_{3z^2-r^2}$, $d_{x^2-y^2} + d_{xy}$). **c** The AFM image of a 10-QL (quintuple layers) Bi_2Se_3 film with a roughness of ~0.5 nm, prepared by the MBE technique (top)[169]. The white scale bar is 100 nm. MOKE (Magneto-optic Kerr Effect) images are used to investigate the current-driven (i.e., SOT-driven) magnetization switching in the Bi_2Se_3/NiFe heterostructure (bottom)[169]. The direction of magnetization is indicated by the white arrow. **d** The schematic drawing of photoinduced AHE driven by a net valley polarization of MoS_2 (i.e., valley Hall effect) (top), and the source-to-drain bias (V_x) dependence of the Hall voltage (V_H) measured for the monolayer MoS_2 transistor device (bottom)[174]. R-L (L-R) indicates the quarter-wave modulation with θ = 45° (−45°) where the polarization is modulated from right-handed to left-handed (from left-handed to right-handed). No net Hall voltage is measured for the linear (half-wave s-p) modulation. No noticeable Hall voltage is observed under R-L modulation for the bilayer MoS_2 case (bilayer, R-L) due to the restored inversion symmetry. Image of **a** reprinted with permission from ref. [160]. Copyright 2019 American Chemical Society. Image of **b** reprinted with permission from ref. [140] Copyright 2011 by the American Physical Society. Image of **c** used from Springer Nature with permission under a CC-BY 4.0[169]. Image of **d** used from ref. [174]. Reprinted with permission from AAAS.

TMD (as shown in Fig. 6b, the maximal spin splitting of the uppermost valence band at the K point is as high as 456 meV for WSe_2 monolayer)[140] and the relatively high SHA measured for TMD ($\theta_{SH} \sim 0.14$ for MoS_2)[167] and topological insulator (TI) (θ_{SH} of up to 425 for $(Bi_{0.5}Sb_{0.5})_2Te_3$ at 1.9 K)[168], further research like the recent work on the FM/TI heterostructure (see Fig. 6c for the SOC-induced magnetization switching observed in Bi_2Se_3 films)[169] can be committed to design, fabricate, and understand the ultralow-power SOT devices enabled by 2D materials. A very recent experimental work on the SOC enhancement in graphene by the proximity effect of WS_2 also provided the great promise for practical device applications due to the electric-field tunability demonstrated[170].

It is highlighted that with semi-metallic TMD materials with reduced crystalline symmetry (e.g., WTe_2[171]), an out-of-plane SOT can be generated to possibly induce magnetization reversal for adjacent magnetic thin films with PMA. The out-of-plane SOT that exists exclusively for currents applied along a low-symmetry axis has already been demonstrated for the (mechanically exfoliated) WTe_2/ (sputtered) Permalloy bi-layer structure[171]. This could provide great flexibility to the SOT device design in terms of directions of charge current injection and spin current detection (unlike the conventional settings of the heavy-metal/FM or high-symmetry TMD/FM structures where the component of spin torque is required to lie within the device plane to induce most effectively the anti-damping switching). Indeed, PMA devices attract much attention recently for high-density magnetic storage device applications due to the fact that they can be scaled to small sizes while maintaining thermal stability[38–40]. This new charge-to-spin conversion mechanism through the TMD's unique crystal symmetries may enable a new strategy for optimizing future spintronic device technologies. The possibility to achieve multi-directional charge-to-spin conversion has also been demonstrated using the low-symmetry TMD material (e.g., $MoTe_2$[172] that appears in semi-metallic, distorted 1T octahedral phases), where both the conventional (i.e., spin polarization is orthogonal to charge current) and unconventional (i.e., spin polarization is parallel to charge current) conversions were detected in the graphene-based NLSV structure[172].

Using the valleys in 2D materials

Fundamentally, the phenomenon of spin polarization in conventional FM metals originates from their unique band structure. In the presence of the 3d energy band splitting with respect to the Fermi level (i.e., $DOS_{majority}$ is mostly filled up being located under the Fermi level while $DOS_{minority}$ is mostly empty being located above the Fermi level), only charge carriers with the majority spin direction can pass through the FM layer because minority spin carriers find enough empty states in FM to scatter into. This separation of charge carriers by spin has been best studied by the anomalous Hall effect (AHE)[173], where the measured Hall voltage

is proportional to the FM's magnetization (c.f., the Hall voltage is proportional to the external magnetic field in the ordinary Hall effect).

Electrons in 2D atomic crystals with a honeycomb lattice structure possess a valley degree of freedom in addition to charge and spin. Like the AHE observed in the FM material, this unique 2D system is predicted to exhibit a similar Hall effect, yet with its sign depending on the valley index. In 2014, Mak et al. reported the observation of so-called valley Hall effect (VHE) in monolayer MoS_2 by illuminating the MoS_2 transistor with circularly polarized light to preferentially excite electrons into a specific valley (Fig. 6d)[174]. In this experiment, electrons from different valleys moved in opposite directions across the MoS_2 sample, with one valley being overrepresented with respect to the other. Valleytronics is a recent research paradigm that makes use of the valley of electrons; the energy bands of certain crystal lattices have two or more minima (i.e., valleys) at equal energies but at different positions in the momentum space. If the number of electrons in these valleys can be precisely controlled, thus producing so-called, valley polarization, it would be possible to create a novel form of valleytronic devices. In this context, monolayer MoS_2 is a promising valleytronic material because its conduction and valence-band edges have two energy-degenerate valleys at the corners (K points) of the first Brillouin zone[175].

Valley polarization in MoS_2

In much the same way that spintronic devices require spin polarization, valley polarization (non-equilibrium charge carrier imbalance between valleys) serves as the essential mechanism to realize the future valleytronic devices. Valley polarization has previously been demonstrated using strain[176,177] or magnetic fields[178–180]. However, none of these approaches allowed dynamic control of charge carriers. More importantly, most of these studies relied on a special device geometry such as quantum well (e.g., AlAs-based two-dimensional electron system). In 2012, Cao et al. performed first-principles calculations on monolayer MoS_2, suggesting that valley polarization is achievable via valley-selective circular dichroism (the two valleys absorb left- and right-handed photons differently) arising from its unique symmetry[181]. In monolayer MoS_2, each Mo sits in the center of a trigonal prismatic cage formed by six sulfur atoms, thus forming the stable honeycomb lattice structure with the broken inversion symmetry. This is the essential condition for valley-selective circular dichroism (VSCD), which is further enhanced by the strong SOC associated with the transition metal's *d* orbitals. Experimental demonstrations of valley polarization in monolayer MoS_2 quickly followed up using the optical pumping technique[182,183].

More recently, valley polarization was generated in MoS_2 by the electrical method, either in a gated bilayer MoS_2 transistor structure (the perpendicular gate bias broke the inversion symmetry in bilayer MoS_2)[184] or using a nonlocal Hall bar device geometry with monolayer MoS_2[185]. It is important to note that the inverse valley Hall effect also made it possible to *detect* valley polarization in MoS_2 electrically[185]. These studies provide researchers with rich insights on generating, controlling, and detecting valley polarization in MoS_2, which can ultimately form the basis of developing the future valleytronic devices based on 2D materials.

Spin-valley coupling in TMD

The broken inversion symmetry together with strong SOC directly leads to spin-valley coupled properties (spin and valley indices of charge carriers are coupled) in monolayer MoS_2 and other group-VI dichalcogenides[175]. From the device perspective, this means that monolayer TMD can provide a unique integrated platform to use valley for better manipulating spin. The strong spin-valley coupling in these 2D materials has two specific consequences for device applications. First, spin and valley relaxation are suppressed at the valence-band edges as flipping each index alone is prohibited by the valley-contrasting spin splitting (0.1–0.5 eV) caused by inversion symmetry breaking. For spintronic devices requiring a long-range spin transport, this large spin-valley coupling may offer a solid mechanism to enhance the spin propagation by controlling the polarization of valleys in 2D materials. Secondly, the valley-dependent optical selection rule (e.g., VSCD[181]) also becomes spin-dependent, thus possibly resulting in photon-induced spin and valley Hall effects. This may be used to produce long-lived spin and valley accumulations on monolayer TMD's boundaries, which is key to the operation of spintronic and valleytronic devices.

CONCLUSIONS

The last few decades of nanomagnetism and spintronics research featured remarkable advances in the development of information storage devices based on multilayers of magnetic metals and insulators. However, high-volume information processing and communication devices, either enabled or assisted by spin, still have a long way to go before commercialization, mainly due to relatively slow progress in semiconductor spintronics (in particular, searching for right materials in right places). Recently, researchers have begun to realize the great potential of 2D materials for advanced spintronic device applications. In this section, several challenges and future perspectives are discussed in terms of material development and device integration for 2D spintronics.

2D magnets

Ferromagnetic order in 2D materials is a coveted property that would allow fundamental studies of spin-dependent properties in low-dimensional nanostructures and further enable novel spintronic device applications. Cr-based vdW crystals such as CrI_3 and $Cr_2Ge_2Te_6$ were reported to be intrinsically ferromagnetic[49,147], showing the great promise to build practical spintronic devices through the use of atomically-thin ferromagnetic materials. The discovery of intrinsic ferromagnetism in these layered structures attracted significant attention in the field because making 2D materials magnetic by defect engineering[109–112] may not be practically applicable (i.e., the induced magnetism is quite weak and lacks robustness). However, the low Curie temperature (T_c) of these materials (T_c is about 45 K for monolayer CrI_3. For a complete list of T_c values reported for a variety of 2D magnetic materials, readers find a recent review article[186] a useful resource) still remained a great challenge in adopting them for practical room-temperature operation of spintronic devices. More recently, room-temperature ferromagnetism was observed in the VSe_2/MoS_2 vdW heterostructure[149], $MnSe_x$ epitaxial films[150], Fe_3GeTe_2[151], and transition metal dihydride (MH_2) monolayers[152], leading the possible pathway to offer spin-polarized carriers through 2D materials at room temperature. For the purpose of electrical spin injection, 2D magnets with half-metallicity (i.e., acts as a metal in one spin direction and an insulator in the other direction)[152] may be worth more research efforts because it offers nearly perfect spin polarization, making it possible to achieve a very high spin injection efficiency in spin transistors or logic switches. For metallic spintronic devices such as MTJs, all-2D MTJ structures (the FM electrodes and the TB are all made of 2D materials) may be constructed by combining with the recent progress in integrating 2D materials as the atomically-thin TB[123]. The device functionality based on 2D magnets already started to be reported, for example, by demonstrating the SOT-induced magnetization switching in Fe_3GeTe_2[187].

Interfacing 2D materials with FM

Although, in principle, 2D materials are expected to be readily interfaced with other classes of materials, including FMs, largely due to its excellent flexibility and other mechanical properties[188], one practical challenge is to prevent oxidation or any other surface contamination of the substrate material during the integration process. Recalling that many existing strategies developed for addressing this issue suffered from degradation of spin polarization in the MTJ structure[122,125–127,132–134], other new approaches may be implemented to better integrate 2D materials with FM thin films. Indeed, researchers have already started growing graphene or h-BN directly on top of the FM catalytic substrate using the carefully-controlled CVD or MBE technique[128–131] instead of relying on *ex-situ* processes such as exfoliation or transfer. Direct growth of TMD materials onto FM substrates has not been demonstrated yet. A recently developed intercalation technique of inserting the FM layer (Co) into an already formed graphene/substrate interface may provide another path for creating an excellent FM/graphene interface[189]. However, the impact of these new processes on the specific spintronic device performance still remains unknown, requiring more advanced studies of applying novel integration processes to create and evaluate the 2D spintronic devices.

Implementation of spin logic

Using spin as a state variable in logic devices provides several advantages over conventional charge-based information processing technologies; non-volatility, faster and more energy-efficient data processing, and increased integration densities. Especially, theorists predict that in spin-based computing, if the rate of spin relaxation is maintained much slower than the switching rate, energy dissipation can be even less than the thermal limit (« 10^{-21} J/bit)[190]. If properly implemented, spintronic computing could better satisfy the rapidly increasing performance needs of emerging abundant-data applications[191]. All-spin logic (ASL)[51] has been considered as one of the most effective ways to implement spin logic with the highest energy-efficiency because both its internal and terminal quantities are spin, requiring no spin-to-charge conversion. To date, despite its great promise, the experimental demonstration of ASL has not been made yet. As already discussed in this article, 2D materials have the potential to address some of the challenges of ASL, such as developing the long-range, high injection-efficiency spin transport channel material.

The concept of ASL, however, continues to evolve towards other device approaches that are more easily implementable or can better represent the emerging computing paradigm. For example, the charge-coupled spin logic (CSL)[58,192] uses robust charge currents for long-distance transport as terminal quantities. In the original proposal of CSL, the SHE was suggested as the write mechanism while MTJ served as the read unit. Recently, the CSL device was experimentally implemented based on a vertically-coupled pair of in-plane and PMA nanomagnets, clearly demonstrating its functionality as a logic gate and a true random number generator[58]. More recently, the newer concept of a probabilistic bit (p-bit)[193] was introduced as an intermediate computing scheme between the conventional bits of digital electronics and the emerging quantum bit (qubit). In the probabilistic spin logic (PSL), low-barrier nanomagnets (i.e., engineered to be purposely unstable) provide a natural physical representation for p-bit, which is the classical entity that fluctuates rapidly between 0 and 1. The PSL may open up new application spaces in an emerging computing hardware domain because of their similarity. For example, the p-bit MTJ, involving the low-barrier nanomagnet as a free layer, can be easily combined with the MOS transistor to create the conventional 1T1R (one transistor-one resistor) circuitry. This could offer an efficient hardware platform to accelerate deep learning computation like the binary stochastic neuron[194]. A new spin logic device concept was also proposed by combining the spin-orbit coupling (for reading) and the magnetoelectric effect (for writing), showing that this magnetoelectric spin-orbit logic exhibits superior energy efficiency than the CMOS technology (by a factor of 10 to 30)[195]. This may benefit greatly from the unique spin properties (large spin Hall angles, long spin lifetime) of 2D materials and their heterostructures[196]. Looking further into how 2D materials can better enable or advance these newer forms of the spin logic device will potentially pave the way for the post-silicon spintronics era.

DATA AVAILABILITY

The authors declare that data supporting the findings of this study are available within the article.

Received: 17 November 2019; Accepted: 8 May 2020;
Published online: 18 June 2020

REFERENCES

1. Frank, D. J. et al. Device scaling limits of Si MOSFETs and their application dependencies. *Proc. IEEE* **89**, 259–288 (2001).
2. Dennard, R. H., Gaensslen, F. H., Rideout, V. L., Bassous, E. & LeBlanc, A. R. Design of ion-implanted MOSFET's with very small physical dimensions. *IEEE J. Solid-State Circuits* **9**, 256–268 (1974).
3. Chang, L. et al. Practical strategies for power-efficient computing technologies. *Proc. IEEE* **98**, 215–236 (2010).
4. Cheung, K. P. In *Proceedings of 2010 International Symposium on VLSI Technology, System and Application*. 72–73 (2010).
5. Lu, H. & Seabaugh, A. Tunnel field-effect transistors: state-of-the-art. *IEEE J. Electron Devices Soc.* **2**, 44–49 (2014).
6. Ionescu, A. M. & Riel, H. Tunnel field-effect transistors as energy-efficient electronic switches. *Nature* **479**, 329 (2011).
7. Choi, W. Y., Park, B.-G., Lee, J. D. & Liu, T.-J. K. Tunneling field-effect transistors (TFETs) with subthreshold swing (SS) less than 60 mV/dec. *IEEE Electron Device Lett.* **28**, 743–745 (2007).
8. Zhang, H. et al. 2D negative capacitance field-effect transistor with organic ferroelectrics. *Nanotechnology* **29**, 244004 (2018).
9. Salahuddin, S. & Datta, S. Use of negative capacitance to provide voltage amplification for low power nanoscale devices. *Nano Lett.* **8**, 405–410 (2008).
10. Alam, M. A., Si, M. & Ye, P. D. A critical review of recent progress on negative capacitance field-effect transistors. *Appl. Phys. Lett.* **114**, 090401 (2019).
11. Das, S. Two dimensional electrostrictive field effect transistor (2D-EFET): a sub-60mV/decade steep slope device with high on current. *Sci. Rep.* **6**, 34811 (2016).
12. van Hemert, T. & Hueting, R. J. Piezoelectric strain modulation in FETs. *IEEE Trans. Electron Devices* **60**, 3265–3270 (2013).
13. Barraud, S. et al. In *2017 IEEE International Electron Devices Meeting (IEDM)*. 29.22.21–29.22.24 (2017).
14. Thomas, S. Nanosheet FETs at 3 nm. *Nat. Electron.* **1**, 613 (2018).
15. Brooks, D. & Martonosi, M. In *Proceedings of the Seventh International Symposium on High-Performance Computer Architecture*. 171–182 (2001).
16. Attia, K. M., El-Hosseini, M. A. & Ali, H. A. Dynamic power management techniques in multi-core architectures: A survey study. *Ain Shams Eng. J.* **8**, 445–456 (2017).
17. Sengupta, A. & Roy, K. Encoding neural and synaptic functionalities in electron spin: a pathway to efficient neuromorphic computing. *Appl. Phys. Rev.* **4**, 041105 (2017).
18. Grollier, J., Querlioz, D. & Stiles, M. D. Spintronic nanodevices for bioinspired computing. *Proc. IEEE* **104**, 2024–2039 (2016).
19. Awschalom, D. D., Bassett, L. C., Dzurak, A. S., Hu, E. L. & Petta, J. R. Quantum spintronics: engineering and manipulating atom-like spins in semiconductors. *Science* **339**, 1174–1179 (2013).
20. Leuenberger, M. N. & Loss, D. Spintronics and quantum computing: switching mechanisms for qubits. *Phys. E: Low.-Dimen. Syst. Nanostruct.* **10**, 452–457 (2001).
21. Baibich, M. N. et al. Giant magnetoresistance of (001) Fe/(001) Cr magnetic superlattices. *Phys. Rev. Lett.* **61**, 2472 (1988).
22. Binasch, G., Grünberg, P., Saurenbach, F. & Zinn, W. Enhanced magnetoresistance in layered magnetic structures with antiferromagnetic interlayer exchange. *Phys. Rev. B* **39**, 4828 (1989).

23. Bruno, P. & Chappert, C. Oscillatory coupling between ferromagnetic layers separated by a nonmagnetic metal spacer. *Phys. Rev. Lett.* **67**, 1602 (1991).
24. Bruno, P. Oscillations of interlayer exchange coupling vs. ferromagnetic-layers thickness. *EPL (Europhys. Lett.)* **23**, 615 (1993).
25. Young Lee, T. et al. Critical switching current and thermal stability of magnetic tunnel junctions with uncompensated CoFeB/Ru/CoFeB synthetic free layers. *J. Appl. Phys.* **113**, 093906 (2013).
26. Hayakawa, J. et al. Current-induced magnetization switching in MgO barrier based magnetic tunnel junctions with CoFeB/Ru/CoFeB synthetic ferrimagnetic free layer. *Jpn. J. Appl. Phys.* **45**, L1057 (2006).
27. Diény, B. Giant magnetoresistance in spin-valve multilayers. *J. Magn. Magn. Mater.* **136**, 335–359 (1994).
28. Dieny, B. et al. Spin-valve effect in soft ferromagnetic sandwiches. *J. Magn. Magn. Mater.* **93**, 101–104 (1991).
29. Moodera, J. S., Kinder, L. R., Wong, T. M. & Meservey, R. Large magnetoresistance at room temperature in ferromagnetic thin film tunnel junctions. *Phys. Rev. Lett.* **74**, 3273 (1995).
30. Ikeda, S. et al. Tunnel magnetoresistance of 604% at 300 K by suppression of Ta diffusion in CoFeB/MgO/CoFeB pseudo-spin-valves annealed at high temperature. *Appl. Phys. Lett.* **93**, 082508 (2008).
31. Berger, L. Emission of spin waves by a magnetic multilayer traversed by a current. *Phys. Rev. B* **54**, 9353 (1996).
32. Slonczewski, J. C. Current-driven excitation of magnetic multilayers. *J. Magn. Magn. Mater.* **159**, L1–L7 (1996).
33. Katine, J., Albert, F., Buhrman, R., Myers, E. & Ralph, D. Current-driven magnetization reversal and spin-wave excitations in Co/Cu/Co pillars. *Phys. Rev. Lett.* **84**, 3149 (2000).
34. Yamaguchi, A. et al. Real-space observation of current-driven domain wall motion in submicron magnetic wires. *Phys. Rev. Lett.* **92**, 077205 (2004).
35. Kiselev, S. I. et al. Microwave oscillations of a nanomagnet driven by a spin-polarized current. *Nature* **425**, 380 (2003).
36. Yuasa, S. & Djayaprawira, D. Giant tunnel magnetoresistance in magnetic tunnel junctions with a crystalline MgO (001) barrier. *J. Phys. D: Appl. Phys.* **40**, R337 (2007).
37. Butler, W. H. Tunneling magnetoresistance from a symmetry filtering effect. *Sci. Technol. Adv. Mater.* **9**, 014106 (2008).
38. Dieny, B. & Chshiev, M. Perpendicular magnetic anisotropy at transition metal/oxide interfaces and applications. *Rev. Mod. Phys.* **89**, 025008 (2017).
39. Tudu, B. & Tiwari, A. Recent developments in perpendicular magnetic anisotropy thin films for data storage applications. *Vacuum* **146**, 329–341 (2017).
40. Yu, J.-X. & Zang, J. Giant perpendicular magnetic anisotropy in Fe/III-V nitride thin films. *Sci. Adv.* **4**, eaar7814 (2018).
41. Inoue, J. & Ohno, H. Taking the hall effect for a spin. *Science* **309**, 2004–2005 (2005).
42. Brodie, B. C. XIII. On the atomic weight of graphite. *Phil. Trans. R. Soc. Lond.* **149**, 249–259 (1859).
43. Novoselov, K. S. et al. Electric field effect in atomically thin carbon films. *Science* **306**, 666–669 (2004).
44. Kong, W. et al. Path towards graphene commercialization from lab to market. *Nat. Nanotechnol.* **14**, 927–938 (2019).
45. Song, L. et al. Large scale growth and characterization of atomic hexagonal boron nitride layers. *Nano Lett.* **10**, 3209–3215 (2010).
46. Manzeli, S., Ovchinnikov, D., Pasquier, D., Yazyev, O. V. & Kis, A. 2D transition metal dichalcogenides. *Nat. Rev. Mater.* **2**, 17033 (2017).
47. Akinwande, D., Petrone, N. & Hone, J. Two-dimensional flexible nanoelectronics. *Nat. Commun.* **5**, 5678 (2014).
48. Xi, X. et al. Ising pairing in superconducting NbSe2 atomic layers. *Nat. Phys.* **12**, 139 (2016).
49. Huang, B. et al. Layer-dependent ferromagnetism in a van der Waals crystal down to the monolayer limit. *Nature* **546**, 270 (2017).
50. Bernstein, K., Cavin, R. K., Porod, W., Seabaugh, A. & Welser, J. Device and architecture outlook for beyond CMOS switches. *Proc. IEEE* **98**, 2169–2184 (2010).
51. Behin-Aein, B., Datta, D., Salahuddin, S. & Datta, S. Proposal for an all-spin logic device with built-in memory. *Nat. Nanotechnol.* **5**, 266 (2010).
52. Dery, H., Dalal, P. & Sham, L. Spin-based logic in semiconductors for reconfigurable large-scale circuits. *Nature* **447**, 573 (2007).
53. Cowburn, R. & Welland, M. Room temperature magnetic quantum cellular automata. *Science* **287**, 1466–1468 (2000).
54. Imre, A. et al. Majority logic gate for magnetic quantum-dot cellular automata. *Science* **311**, 205–208 (2006).
55. Carlton, D. B., Emley, N. C., Tuchfeld, E. & Bokor, J. Simulation studies of nanomagnet-based logic architecture. *Nano Lett.* **8**, 4173–4178 (2008).
56. Allwood, D. A. et al. Magnetic domain-wall logic. *Science* **309**, 1688–1692 (2005).
57. Murapaka, C., Sethi, P., Goolaup, S. & Lew, W. S. Reconfigurable logic via gate controlled domain wall trajectory in magnetic network structure. *Sci. Rep.* **6**, 20130 (2016).
58. Debashis, P. & Chen, Z. Experimental Demonstration of a Spin Logic Device with Deterministic and Stochastic Mode of Operation. *Sci. Rep.* **8**, 11405 (2018).
59. Salahuddin, S. & Datta, S. Interacting systems for self-correcting low power switching. *Appl. Phys. Lett.* **90**, 093503 (2007).
60. Behin-Aein, B., Salahuddin, S. & Datta, S. Switching energy of ferromagnetic logic bits. *IEEE Trans. Nanotechnol.* **8**, 505–514 (2009).
61. Johnson, M. & Silsbee, R. H. Interfacial charge-spin coupling: Injection and detection of spin magnetization in metals. *Phys. Rev. Lett.* **55**, 1790 (1985).
62. Jedema, F. J., Filip, A. & Van Wees, B. Electrical spin injection and accumulation at room temperature in an all-metal mesoscopic spin valve. *Nature* **410**, 345 (2001).
63. Idzuchi, H., Fukuma, Y. & Otani, Y. Spin transport in non-magnetic nano-structures induced by non-local spin injection. *Phys. E: Low.-dimensional Syst. Nanostruct.* **68**, 239–263 (2015).
64. Han, W., Kawakami, R. K., Gmitra, M. & Fabian, J. Graphene spintronics. *Nat. Nanotechnol.* **9**, 794 (2014).
65. Roche, S. et al. Graphene spintronics: the European Flagship perspective. *2D Mater.* **2**, 030202 (2015).
66. Gmitra, M., Konschuh, S., Ertler, C., Ambrosch-Draxl, C. & Fabian, J. Band-structure topologies of graphene: Spin-orbit coupling effects from first principles. *Phys. Rev. B* **80**, 235431 (2009).
67. Boettger, J. & Trickey, S. First-principles calculation of the spin-orbit splitting in graphene. *Phys. Rev. B* **75**, 121402 (2007).
68. Bolotin, K. I. et al. Ultrahigh electron mobility in suspended graphene. *Solid State Commun.* **146**, 351–355 (2008).
69. Ji, Y., Hoffmann, A., Jiang, J., Pearson, J. & Bader, S. Non-local spin injection in lateral spin valves. *J. Phys. D: Appl. Phys.* **40**, 1280 (2007).
70. Yang, T., Kimura, T. & Otani, Y. Giant spin-accumulation signal and pure spin-current-induced reversible magnetization switching. *Nat. Phys.* **4**, 851 (2008).
71. Tombros, N., Jozsa, C., Popinciuc, M., Jonkman, H. T. & Van Wees, B. J. Electronic spin transport and spin precession in single graphene layers at room temperature. *Nature* **448**, 571 (2007).
72. Žutić, I., Fabian, J. & Sarma, S. D. Spintronics: fundamentals and applications. *Rev. Mod. Phys.* **76**, 323 (2004).
73. Cubukcu, M. et al. Ferromagnetic tunnel contacts to graphene: contact resistance and spin signal. *J. Appl. Phys.* **117**, 083909 (2015).
74. Jedema, F., Heersche, H., Filip, A., Baselmans, J. & Van Wees, B. Electrical detection of spin precession in a metallic mesoscopic spin valve. *Nature* **416**, 713 (2002).
75. Huang, B., Monsma, D. J. & Appelbaum, I. Coherent spin transport through a 350 micron thick silicon wafer. *Phys. Rev. Lett.* **99**, 177209 (2007).
76. Schmidt, G., Ferrand, D., Molenkamp, L., Filip, A. & Van Wees, B. Fundamental obstacle for electrical spin injection from a ferromagnetic metal into a diffusive semiconductor. *Phys. Rev. B* **62**, R4790 (2000).
77. Drögeler, M. et al. Spin lifetimes exceeding 12 ns in graphene nonlocal spin valve devices. *Nano Lett.* **16**, 3533–3539 (2016).
78. Ingla-Aynés, J., Meijerink, R. J. & Wees, B. J. V. Eighty-eight percent directional guiding of spin currents with 90 μm relaxation length in bilayer graphene using carrier drift. *Nano Lett.* **16**, 4825–4830 (2016).
79. Dankert, A., Kamalakar, M. V., Bergsten, J. & Dash, S. P. Spin transport and precession in graphene measured by nonlocal and three-terminal methods. *Appl. Phys. Lett.* **104**, 192403 (2014).
80. Kamalakar, M. V., Groenveld, C., Dankert, A. & Dash, S. P. Long distance spin communication in chemical vapour deposited graphene. *Nat. Commun.* **6**, 6766 (2015).
81. Volmer, F. et al. Role of MgO barriers for spin and charge transport in Co/MgO/graphene nonlocal spin-valve devices. *Phys. Rev. B* **88**, 161405 (2013).
82. Han, W. et al. Tunneling spin injection into single layer graphene. *Phys. Rev. Lett.* **105**, 167202 (2010).
83. Han, W. & Kawakami, R. K. Spin relaxation in single-layer and bilayer graphene. *Phys. Rev. Lett.* **107**, 047207 (2011).
84. Yamaguchi, T. et al. Electrical spin injection into graphene through monolayer hexagonal boron nitride. *Appl. Phys. Express* **6**, 073001 (2013).
85. Yamaguchi, T., Masubuchi, S., Iguchi, K., Moriya, R. & Machida, T. Tunnel spin injection into graphene using Al2O3 barrier grown by atomic layer deposition on functionalized graphene surface. *J. Magn. Magn. Mater.* **324**, 849–852 (2012).
86. Popinciuc, M. et al. Electronic spin transport in graphene field-effect transistors. *Phys. Rev. B* **80**, 214427 (2009).
87. Guimarães, M. H. et al. Spin transport in high-quality suspended graphene devices. *Nano Lett.* **12**, 3512–3517 (2012).

88. Friedman, A. L., van't Erve, O. M., Li, C. H., Robinson, J. T. & Jonker, B. T. Homoepitaxial tunnel barriers with functionalized graphene-on-graphene for charge and spin transport. *Nat. Commun.* **5**, 3161 (2014).
89. Kamalakar, M. V., Dankert, A., Kelly, P. J. & Dash, S. P. Inversion of spin signal and spin filtering in ferromagnet|hexagonal boron nitride-graphene van der Waals heterostructures. *Sci. Rep.* **6**, 1–9 (2016).
90. Gurram, M., Omar, S. & van Wees, B. J. Bias induced up to 100% spin-injection and detection polarizations in ferromagnet/bilayer-hBN/graphene/hBN heterostructures. *Nat. Commun.* **8**, 1–7 (2017).
91. Zhu, T. et al. Probing tunneling spin injection into graphene via bias dependence. *Phys. Rev. B* **98**, 054412 (2018).
92. Zomer, P., Guimaraes, M., Tombros, N. & Van Wees, B. Long-distance spin transport in high-mobility graphene on hexagonal boron nitride. *Phys. Rev. B* **86**, 161416 (2012).
93. Drögeler, M. et al. Nanosecond spin lifetimes in single-and few-layer graphene–hBN heterostructures at room temperature. *Nano Lett.* **14**, 6050–6055 (2014).
94. Dean, C. R. et al. Boron nitride substrates for high-quality graphene electronics. *Nat. Nanotechnol.* **5**, 722 (2010).
95. Geim, A. K. & Grigorieva, I. V. Van der Waals heterostructures. *Nature* **499**, 419–425 (2013).
96. Yankowitz, M., Ma, Q., Jarillo-Herrero, P. & LeRoy, B. J. van der Waals heterostructures combining graphene and hexagonal boron nitride. *Nat. Rev. Phys* **1**, 112–125 (2019).
97. Gurram, M., Omar, S. & van Wees, B. J. Electrical spin injection, transport, and detection in graphene-hexagonal boron nitride van der Waals heterostructures: progress and perspectives. *2D Mater.* **5**, 032004 (2018).
98. Elliott, R. J. Theory of the effect of spin-orbit coupling on magnetic resonance in some semiconductors. *Phys. Rev.* **96**, 266 (1954).
99. Dyakonov, M. & Perel, V. Spin relaxation of conduction electrons in noncentrosymmetric semiconductors. *Sov. Phys. Solid State, Ussr* **13**, 3023–3026 (1972).
100. Yang, T.-Y. et al. Observation of long spin-relaxation times in bilayer graphene at room temperature. *Phys. Rev. Lett.* **107**, 047206 (2011).
101. Gebeyehu, Z. M. et al. Spin communication over 30 μm long channels of chemical vapor deposited graphene on SiO2. *2D Mater.* **6**, 034003 (2019).
102. Khokhriakov, D., Karpiak, B., Hoque, A. M. & Dash, S. P. Two-dimensional spintronic circuit architectures on large scale graphene. *Carbon* **161**, 892–899 (2020).
103. Dlubak, B. et al. Highly efficient spin transport in epitaxial graphene on SiC. *Nat. Phys.* **8**, 557 (2012).
104. Huertas-Hernando, D., Guinea, F. & Brataas, A. Spin relaxation times in disordered graphene. *Eur. Phys. J. Spec. Top.* **148**, 177–181 (2007).
105. Ertler, C., Konschuh, S., Gmitra, M. & Fabian, J. Electron spin relaxation in graphene: the role of the substrate. *Phys. Rev. B* **80**, 041405 (2009).
106. Park, C.-H., Yang, L., Son, Y.-W., Cohen, M. L. & Louie, S. G. Anisotropic behaviours of massless Dirac fermions in graphene under periodic potentials. *Nat. Phys.* **4**, 213 (2008).
107. Silva, E. et al. Thickness dependence of the magnetic anisotropy and dynamic magnetic response of ferromagnetic NiFe films. *J. Phys. D: Appl. Phys.* **50**, 185001 (2017).
108. Jensen, P., Dreyssé, H. & Bennemann, K. Calculation of the film-thickness-dependence of the Curie temperature in thin transition metal films. *EPL (Europhys. Lett.)* **18**, 463 (1992).
109. Yazyev, O. V. & Helm, L. Defect-induced magnetism in graphene. *Phys. Rev. B* **75**, 125408 (2007).
110. McCreary, K. M., Swartz, A. G., Han, W., Fabian, J. & Kawakami, R. K. Magnetic moment formation in graphene detected by scattering of pure spin currents. *Phys. Rev. Lett.* **109**, 186604 (2012).
111. Nair, R. et al. Spin-half paramagnetism in graphene induced by point defects. *Nat. Phys.* **8**, 199 (2012).
112. Hong, X., Zou, K., Wang, B., Cheng, S.-H. & Zhu, J. Evidence for spin-flip scattering and local moments in dilute fluorinated graphene. *Phys. Rev. Lett.* **108**, 226602 (2012).
113. Elias, D. C. et al. Control of graphene's properties by reversible hydrogenation: evidence for graphane. *Science* **323**, 610–613 (2009).
114. Nair, R. R. et al. Fluorographene: a two-dimensional counterpart of Teflon. *Small* **6**, 2877–2884 (2010).
115. Lieb, E. H. Two theorems on the Hubbard model. *Phys. Rev. Lett.* **62**, 1201 (1989).
116. Hu, W. et al. Room-temperature magnetism and tunable energy gaps in edge-passivated zigzag graphene quantum dots. *npj 2D Mater. Appl.* **3**, 17 (2019).
117. Ugeda, M. M., Brihuega, I., Guinea, F. & Gómez-Rodríguez, J. M. Missing atom as a source of carbon magnetism. *Phys. Rev. Lett.* **104**, 096804 (2010).
118. Chen, E. et al. Advances and future prospects of spin-transfer torque random access memory. *IEEE Trans. Magn.* **46**, 1873–1878 (2010).
119. Ahn, E. C., Wong, H.-S. P. & Pop, E. Carbon nanomaterials for non-volatile memories. *Nat. Rev. Mater.* **3**, 18009 (2018).
120. Yan, H., Cherian, H. R., Ahn, E. C., Qian, X. & Duan, L. iCELIA: a full-stack framework for STT-MRAM-based deep learning acceleration. *IEEE Trans. Parallel Distrib. Syst.* **31**, 408–422 (2019).
121. Karpan, V. et al. Graphite and graphene as perfect spin filters. *Phys. Rev. Lett.* **99**, 176602 (2007).
122. Mohiuddin, T. M. et al. Graphene in multilayered CPP spin valves. *IEEE Trans. Magn.* **44**, 2624–2627 (2008).
123. Piquemal-Banci, M. et al. 2D-MTJs: introducing 2D materials in magnetic tunnel junctions. *J. Phys. D: Appl. Phys.* **50**, 203002 (2017).
124. Cobas, E., Friedman, A. L., van't Erve, O. M., Robinson, J. T. & Jonker, B. T. Graphene as a tunnel barrier: graphene-based magnetic tunnel junctions. *Nano Lett.* **12**, 3000–3004 (2012).
125. Park, J.-H. & Lee, H.-J. Out-of-plane magnetoresistance in ferromagnet/graphene/ferromagnet spin-valve junctions. *Phys. Rev. B* **89**, 165417 (2014).
126. Li, F., Li, T. & Guo, X. Vertical graphene spin valves based on La2/3Sr1/3MnO3 electrodes. *ACS Appl. Mater. Interfaces* **6**, 1187–1192 (2014).
127. Dankert, A., Kamalakar, M. V., Wajid, A., Patel, R. S. & Dash, S. P. Tunnel magnetoresistance with atomically thin two-dimensional hexagonal boron nitride barriers. *Nano Res.* **8**, 1357–1364 (2015).
128. Piquemal-Banci, M. et al. Magnetic tunnel junctions with monolayer hexagonal boron nitride tunnel barriers. *Appl. Phys. Lett.* **108**, 102404 (2016).
129. Tonkikh, A. et al. Structural and electronic properties of epitaxial multilayer h-BN on Ni (111) for spintronics applications. *Sci. Rep.* **6**, 23547 (2016).
130. Weatherup, R. S., Dlubak, B. & Hofmann, S. Kinetic control of catalytic CVD for high-quality graphene at low temperatures. *ACS Nano* **6**, 9996–10003 (2012).
131. Weatherup, R. S. et al. On the mechanisms of Ni-catalysed graphene chemical vapour deposition. *ChemPhysChem* **13**, 2544–2549 (2012).
132. Wang, W. et al. Spin-valve effect in NiFe/MoS2/NiFe junctions. *Nano Lett.* **15**, 5261–5267 (2015).
133. Wu, H.-C. et al. Spin-dependent transport properties of Fe3O4/MoS2/Fe3O4 junctions. *Sci. Rep.* **5**, 15984 (2015).
134. Iqbal, M. Z., Iqbal, M. W., Siddique, S., Khan, M. F. & Ramay, S. M. Room temperature spin valve effect in NiFe/WS2/Co junctions. *Sci. Rep.* **6**, 21038 (2016).
135. Datta, S. & Das, B. Electronic analog of the electro-optic modulator. *Appl. Phys. Lett.* **56**, 665–667 (1990).
136. Koo, H. C. et al. Control of spin precession in a spin-injected field effect transistor. *Science* **325**, 1515–1518 (2009).
137. Chuang, P. et al. All-electric all-semiconductor spin field-effect transistors. *Nat. Nanotechnol.* **10**, 35 (2015).
138. Sugahara, S. & Nitta, J. Spin-transistor electronics: an overview and outlook. *Proc. IEEE* **98**, 2124–2154 (2010).
139. Yan, W. et al. A two-dimensional spin field-effect switch. *Nat. Commun.* **7**, 13372 (2016).
140. Zhu, Z., Cheng, Y. & Schwingenschlögl, U. Giant spin-orbit-induced spin splitting in two-dimensional transition-metal dichalcogenide semiconductors. *Phys. Rev. B* **84**, 153402 (2011).
141. Castellanos-Gomez, A. et al. Deterministic transfer of two-dimensional materials by all-dry viscoelastic stamping. *2D Mater.* **1**, 011002 (2014).
142. Dankert, A. & Dash, S. P. Electrical gate control of spin current in van der Waals heterostructures at room temperature. *Nat. Commun.* **8**, 16093 (2017).
143. Cummings, A. W., Garcia, J. H., Fabian, J. & Roche, S. Giant spin lifetime anisotropy in graphene induced by proximity effects. *Phys. Rev. Lett.* **119**, 206601 (2017).
144. Ghiasi, T. S., Ingla-Aynés, J., Kaverzin, A. A. & van Wees, B. J. Large proximity-induced spin lifetime anisotropy in transition-metal dichalcogenide/graphene heterostructures. *Nano Lett.* **17**, 7528–7532 (2017).
145. Benítez, L. A. et al. Strongly anisotropic spin relaxation in graphene–transition metal dichalcogenide heterostructures at room temperature. *Nat. Phys.* **14**, 303–308 (2018).
146. Jiang, S., Li, L., Wang, Z., Shan, J. & Mak, K. F. Spin tunnel field-effect transistors based on two-dimensional van der Waals heterostructures. *Nat. Electron.* **2**, 159 (2019).
147. Gong, C. et al. Discovery of intrinsic ferromagnetism in two-dimensional van der Waals crystals. *Nature* **546**, 265 (2017).
148. Lee, J.-U. et al. Ising-type magnetic ordering in atomically thin FePS3. *Nano Lett.* **16**, 7433–7438 (2016).
149. Bonilla, M. et al. Strong room-temperature ferromagnetism in VSe2 monolayers on van der Waals substrates. *Nat. Nanotechnol.* **13**, 289 (2018).
150. O'Hara, D. J. et al. Room temperature intrinsic ferromagnetism in epitaxial manganese selenide films in the monolayer limit. *Nano Lett.* **18**, 3125–3131 (2018).
151. Deng, Y. et al. Gate-tunable room-temperature ferromagnetism in two-dimensional Fe 3 GeTe 2. *Nature* **563**, 94 (2018).

152. Wu, Q., Zhang, Y., Zhou, Q., Wang, J. & Zeng, X. C. Transition-metal dihydride monolayers: a new family of two-dimensional ferromagnetic materials with intrinsic room-temperature half-metallicity. *J. Phys. Chem. Lett.* **9**, 4260–4266 (2018).
153. Jiang, S., Shan, J. & Mak, K. F. Electric-field switching of two-dimensional van der Waals magnets. *Nat. Mater.* **17**, 406 (2018).
154. Song, T. et al. Giant tunneling magnetoresistance in spin-filter van der Waals heterostructures. *Science* **360**, 1214–1218 (2018).
155. Wang, Z. et al. Very large tunneling magnetoresistance in layered magnetic semiconductor CrI3. *Nat. Commun.* **9**, 2516 (2018).
156. Klein, D. R. et al. Probing magnetism in 2D van der Waals crystalline insulators via electron tunneling. *Science* **360**, 1218–1222 (2018).
157. Novoselov, K. S. et al. Two-dimensional gas of massless Dirac fermions in graphene. *Nature* **438**, 197 (2005).
158. Zhang, Y., Tan, Y.-W., Stormer, H. L. & Kim, P. Experimental observation of the quantum Hall effect and Berry's phase in graphene. *Nature* **438**, 201 (2005).
159. Hirsch, J. Spin hall effect. *Phys. Rev. Lett.* **83**, 1834 (1999).
160. Safeer, C. et al. Room-temperature spin Hall effect in graphene/MoS2 van der Waals heterostructures. *Nano Lett.* **19**, 1074–1082 (2019).
161. Garcia, J. H., Cummings, A. W. & Roche, S. Spin Hall effect and weak antilocalization in graphene/transition metal dichalcogenide heterostructures. *Nano Lett.* **17**, 5078–5083 (2017).
162. Offidani, M., Milletarì, M., Raimondi, R. & Ferreira, A. Optimal charge-to-spin conversion in graphene on transition-metal dichalcogenides. *Phys. Rev. Lett.* **119**, 196801 (2017).
163. Ghiasi, T. S., Kaverzin, A. A., Blah, P. J. & van Wees, B. J. Charge-to-spin conversion by the rashba–edelstein effect in two-dimensional van der waals heterostructures up to room temperature. *Nano Lett.* **19**, 5959–5966 (2019).
164. Liu, L. et al. Spin-torque switching with the giant spin Hall effect of tantalum. *Science* **336**, 555–558 (2012).
165. Liu, L., Pai, C.-F., Ralph, D. & Buhrman, R. Magnetic oscillations driven by the spin Hall effect in 3-terminal magnetic tunnel junction devices. *Phys. Rev. Lett.* **109**, 186602 (2012).
166. Deng, Y., Yang, M., Ji, Y. & Wang, K. Estimating spin Hall angle in heavy metal/ferromagnet heterostructures. *J. Magn. Magn. Mater.* **496**, 165920 (2019).
167. Shao, Q. et al. Strong Rashba-Edelstein effect-induced spin–orbit torques in monolayer transition metal dichalcogenide/ferromagnet bilayers. *Nano Lett.* **16**, 7514–7520 (2016).
168. Fan, Y. et al. Magnetization switching through giant spin–orbit torque in a magnetically doped topological insulator heterostructure. *Nat. Mater.* **13**, 699 (2014).
169. Wang, Y. et al. Room temperature magnetization switching in topological insulator-ferromagnet heterostructures by spin-orbit torques. *Nat. Commun.* **8**, 1–6 (2017).
170. Benítez, L. A. et al. Tunable room-temperature spin galvanic and spin Hall effects in van der Waals heterostructures. *Nat. Mater.* **19**, 170–175 (2020).
171. MacNeill, D. et al. Control of spin–orbit torques through crystal symmetry in WTe 2/ferromagnet bilayers. *Nat. Phys.* **13**, 300–305 (2017).
172. Safeer, C. et al. Large multidirectional spin-to-charge conversion in low-symmetry semimetal MoTe2 at room temperature. *Nano Lett.* **19**, 8758–8766 (2019).
173. Nagaosa, N., Sinova, J., Onoda, S., MacDonald, A. H. & Ong, N. P. Anomalous hall effect. *Rev. Mod. Phys.* **82**, 1539 (2010).
174. Mak, K. F., McGill, K. L., Park, J. & McEuen, P. L. The valley Hall effect in MoS2 transistors. *Science* **344**, 1489–1492 (2014).
175. Xiao, D., Liu, G.-B., Feng, W., Xu, X. & Yao, W. Coupled spin and valley physics in monolayers of MoS2 and other group-VI dichalcogenides. *Phys. Rev. Lett.* **108**, 196802 (2012).
176. Gunawan, O. et al. Valley susceptibility of an interacting two-dimensional electron system. *Phys. Rev. Lett.* **97**, 186404 (2006).
177. Takashina, K., Ono, Y., Fujiwara, A., Takahashi, Y. & Hirayama, Y. Valley polarization in Si (100) at zero magnetic field. *Phys. Rev. Lett.* **96**, 236801 (2006).
178. Shkolnikov, Y., De Poortere, E., Tutuc, E. & Shayegan, M. Valley splitting of AlAs two-dimensional electrons in a perpendicular magnetic field. *Phys. Rev. Lett.* **89**, 226805 (2002).
179. Bishop, N. et al. Valley polarization and susceptibility of composite fermions around a filling factor $v=3/2$. *Phys. Rev. Lett.* **98**, 266404 (2007).
180. Zhu, Z., Collaudin, A., Fauqué, B., Kang, W. & Behnia, K. Field-induced polarization of Dirac valleys in bismuth. *Nat. Phys.* **8**, 89 (2012).
181. Cao, T. et al. Valley-selective circular dichroism of monolayer molybdenum disulphide. *Nat. Commun.* **3**, 887 (2012).
182. Zeng, H., Dai, J., Yao, W., Xiao, D. & Cui, X. Valley polarization in MoS2 monolayers by optical pumping. *Nat. Nanotechnol.* **7**, 490 (2012).
183. Mak, K. F., He, K., Shan, J. & Heinz, T. F. Control of valley polarization in monolayer MoS2 by optical helicity. *Nat. Nanotechnol.* **7**, 494 (2012).
184. Lee, J., Mak, K. F. & Shan, J. Electrical control of the valley Hall effect in bilayer MoS2 transistors. *Nat. Nanotechnol.* **11**, 421 (2016).
185. Hung, T. Y., Camsari, K. Y., Zhang, S., Upadhyaya, P. & Chen, Z. Direct observation of valley-coupled topological current in MoS2. *Sci. Adv.* **5**, eaau6478 (2019).
186. Lin, X., Yang, W., Wang, K. L. & Zhao, W. Two-dimensional spintronics for low-power electronics. *Nat. Electron.* **2**, 274–283 (2019).
187. Wang, X. et al. Current-driven magnetization switching in a van der Waals ferromagnet Fe3GeTe2. arXiv preprint arXiv:1902.05794 (2019).
188. Kim, J. H., Jeong, J. H., Kim, N., Joshi, R. & Lee, G.-H. Mechanical properties of two-dimensional materials and their applications. *J. Phys. D: Appl. Phys.* **52**, 083001 (2018).
189. Rougemaille, N. et al. Perpendicular magnetic anisotropy of cobalt films intercalated under graphene. *Appl. Phys. Lett.* **101**, 142403 (2012).
190. Nikonov, D. E., Bourianoff, G. I. & Gargini, P. A. Power dissipation in spintronic devices out of thermodynamic equilibrium. *J. Superconductivity Nov. Magn.* **19**, 497–513 (2006).
191. Chen, M., Mao, S., Zhang, Y. & Leung, V. C. Big data: related technologies, challenges and future prospects. (Springer, 2014).
192. Datta, S., Salahuddin, S. & Behin-Aein, B. Non-volatile spin switch for Boolean and non-Boolean logic. *Appl. Phys. Lett.* **101**, 252411 (2012).
193. Camsari, K. Y., Sutton, B. M. & Datta, S. p-bits for probabilistic spin logic. *Appl. Phys. Rev.* **6**, 011305 (2019).
194. Nedjah, N. & de Macedo Mourelle, L. Reconfigurable hardware for neural networks: binary versus stochastic. *Neural Comput. Appl.* **16**, 249–255 (2007).
195. Manipatruni, S. et al. Scalable energy-efficient magnetoelectric spin–orbit logic. *Nature* **565**, 35–42 (2019).
196. Pham, V. T. et al. Spin–orbit magnetic state readout in scaled ferromagnetic/heavy metal nanostructures. *Nat. Electron.* https://doi.org/10.1038/s41928-020-0395-y (2020).

ACKNOWLEDGEMENTS

This work was supported by the UT System Faculty Science and Technology Acquisition and Retention (STARs), the National Science Foundation (NSF) grant 1929118, and the Air Force Office of Scientific Research (AFOSR) grant FA9550-19-1-0085.

AUTHOR CONTRIBUTIONS

E.C.A. conceived the idea for the review article and wrote the manuscript.

COMPETING INTERESTS

The author declares no competing interests.

ADDITIONAL INFORMATION

Correspondence and requests for materials should be addressed to E.C.A.

Reprints and permission information is available at http://www.nature.com/reprints

Publisher's note Springer Nature remains neutral with regard to jurisdictional claims in published maps and institutional affiliations.

Open Access This article is licensed under a Creative Commons Attribution 4.0 International License, which permits use, sharing, adaptation, distribution and reproduction in any medium or format, as long as you give appropriate credit to the original author(s) and the source, provide a link to the Creative Commons license, and indicate if changes were made. The images or other third party material in this article are included in the article's Creative Commons license, unless indicated otherwise in a credit line to the material. If material is not included in the article's Creative Commons license and your intended use is not permitted by statutory regulation or exceeds the permitted use, you will need to obtain permission directly from the copyright holder. To view a copy of this license, visit http://creativecommons.org/licenses/by/4.0/.

© The Author(s) 2020